Numerical Study of Multiphase Hybrid Gyro-tactic Nanofluid Flow through Porous Convergent Pipe with Injection and Suction

David Chepkonga, *Member, IAENG,* Mathew Kinyanjui, Roy Kiogora, and Kang'ethe Giterere.

Abstract*—Due to the continued exploitation of oil fields, oil is getting difficult to extract from its source due to the inefficiency in the available methods that are currently being used to extract it. This study is aimed at solving the issue through enabling the oil that remains unexploited by the existing methods to be exploited. The novelty of this study is the consideration of microorganisms, hybrid nanoparticles, non-Newtonian fluids, a power law model and inclined magnetic fields. The flow is governed by nonlinear partial differential equations. That are transformed to ordinary differential equations by using similarity transformation and solved numerically via the spectral relaxation method using Chebyshev–Gauss–Lobatto grid points, then implemented in Matlab to obtain the profiles for the various flow variables: velocity, temperature, concentration and microorganism density profiles. The results indicate that the flow parameters significantly influence the flow behavior. The velocity of the fluid increases with Reynolds number, Hartman number, Grashof number and Darcy's parameter. The temperature of the fluid increases with Reynolds number, Hartman number, Eckert number, Unsteadiness parameter, Grashof number, Darcy's parameter, Joule heating parameter and decreases with chemical reaction and Radiaton parameters. Nanoparticle concentration increases with Reynolds number, Hartman number, Microbial Grashof number, Joule heating parameter, Prandtl number and Schmidt number, while it decreases with chemical reaction parameter and thermophoresis. Microbial density increases with Reynolds number and Hartmann number and decreases with Lewis and Peclet number. These insights offer valuable guidance to improve oil recovery by indicating clearly the parameters that are essential in facilitating greater oil recovery.

***Index Terms*—multiphase, hybrid, gyro-tactic, numerical solution, nanofluid, spectral methods**

NOMENCLATURES

V- Velocity of the fluid, meters per second (m/s)
t- Time, seconds (s)
P- Pressure, Newtons per square meter (N/m²)
Q- Planar volumetric flow rate, square meters per second (m²/s)
K- Constant of thermophoretic diffusivity
C_p- Specific heat capacity, Joules per kilogram per Kelvin ($J \cdot kg^{-1} \cdot K^{-1}$)
T- Temperature of the fluid, Kelvin (K)
C- Concentration of the fluid, kilograms per cubic meter (kg/m³)
D- Mass diffusivity, square meters per second (m²/s)
x, y, z- Cartesian coordinate system
r, θ**, z**- Cylindrical coordinate system
D_{nf}- Mass diffusivity of nanoparticles, square meters per second (m²/s)
S_{nf}- Concentration source term of nanoparticles
D_m- Mass diffusivity of microorganisms, square meters per second (m²/s)
S_m- Concentration source term of microorganisms
T_∞- Ambient temperature of the fluid, Kelvin (K)
C_∞- Ambient concentration of the fluid, kilograms per cubic meter (kg/m³)

ABBREVIATIONS

CO_2- Carbon dioxide
MEOR- Microbial-Enhanced Oil Recovery
SRM- Spectral relaxation method
MATLAB- Matrix Laboratory
ODEs- Ordinary differential equations
PDEs- Partial differential equations

I. Introduction

As the world population is growing, available oil resources are becoming scarce; thus, the need to provide clean energy without affecting the environment is inevitable. The primary energy resource in the current decade is still hydrocarbons. Renewable energy sources are yet to be developed and therefore cannot meet energy requirements, as they require a great deal of research and development in terms of efficiency and cost to make them viable replacements for hydrocarbons.

Hydrocarbons remain the primary energy source due to underdeveloped renewable alternatives. However, global energy demand rises amidst unpredictable oil prices. To sustainably meet this demand, there is a growing focus on improving oil recovery from mature fields using a cost-effective and eco-friendly approach. Even a small increase in the recovery percentage could produce significant boosts in oil supply, given the challenge of extracting residues from existing reservoirs amid the dwindling discoveries of new fields (Nikolova et al.) [1].

As oil reserves diminish, extraction methods become more costly and environmentally risky as a result of chemical usage. Traditional extraction techniques, primarily primary and secondary methods, yield only a fraction of the available oil.

Manuscript received June 15, 2024; revised December 6, 2024.

David Chepkonga is a PhD candidate of Jomo Kenyatta University of Agriculture and Technology, Nairobi, Kenya. (phone: +254716388191;; e-mail: chepkonga.david@jkuat.ac.ke).

Mathew Kinyanjui is a Professor of Mathematics Department, Jomo Kenyatta University of Agriculture and Technology, Nairobi, Kenya. (e-mail: mathewkiny@jkuat.ac.ke).

Roy Kiogora is a Senior Lecturer in Mathematics Department, Jomo Kenyatta University of Agriculture and Technology, Nairobi, Kenya. (e-mail: prkiogora@fsc.jkuat.ac.ke).

Kang'ethe Giterere is a Senior Lecturer in Mathematics Department, Jomo Kenyatta University of Agriculture and Technology, Nairobi, Kenya. (e-mail: kngit@jkuat.ac.ke).

To enhance extraction, tertiary methods, such as enhanced oil recovery, are employed. Primary extraction is based on the rise or pump jacks of natural hydrocarbons, but recovers only a small portion (around 5–15%) of accessible oil, leaving significant reserves untapped.

Gas injection, while effective, requires costly compressors to convert gas to liquid. The use of carbon (IV) oxide CO_2 causes corrosion in pipes, poses long-term economic challenges. Enhanced oil recovery (EOR) methods offer the most efficient recovery, targeting changes in oil properties to enhance extraction. EOR encompasses: thermal recovery, that is, using heat to reduce viscosity; gas injection, using CO_2 to reduce viscosity; and chemical injection, aimed at reducing surface tension, which goes a long way in enhancing water flooding efficiency.

Microbial-Enhanced Oil Recovery (MEOR) involves injecting live microorganisms and nutrients into wells to stimulate oil production, with microbial growth influenced by factors like pressure, porosity, pH, and salinity. MEOR can yield up to 50% of residual oil, surpassing other methods.

The study aims at improving oil recovery using thermal energy, magnetic fields, and gyro-tactic microorganisms, investigating their impact on density, viscosity, phase behavior, and hybrid nanoparticle behavior to improve recovery processes.

Ahmad et al. [2] carried out a study on nanofluid flow comprising gyro-tactic microorganisms past a porous horizontal surface. The dispersal of microorganisms was observed to improve and reinforce thermal efficiency of energy systems. The porous media improved thermal efficiency significantly. They employed similarity transformation to transform the PDEs into ODEs and thereby applied the Successive Over Relaxation method. The resulting equations were implemented in Matlab. The results showed that bioconvection peclet number and microorganisms concentration enhances the density of motile microorganisms.

Alabdulhadi et al. [3] carried out a study on hybrid nanofluid flow and heat transfer through an inclined surface. The governing equations were solved using MATLAB Bvp4c. The results from this study showed that an increase in magnetic parameter substantially improves the heat transfer and also the skin friction coefficient. It was noted that increasing nanoparticle volume fraction for gold improves heat transfer and diminishes the mass transfer.

Armstrong et al. [4] performed an experiment to study the effects of pore morphology on microbial enhanced oil recovery. They carried out the study experimentally with a view of reducing the inter-facial tension. The results showed that oil recovery was enhanced with an increase in the amount of biomass.

Azam et al. [5] carried out a study on Bioconvection and activation energy on radiative sutter by melting nanomaterial with gyro-tactic microorganisms. They used Runge–Kutta–Fehlberg as the numerical method of solution. The study highlighted that microorganisms field and nanoparticle concentration are depressed by magnetic parameter. The study also noted that the rate of heat transfer was improved by magnetic parameter.

Behlülgil et al. [6] examined the microbial enhanced oil recovery using experimental conditions to develop a mathematical model. Results showed increasing bacterial concentration over time as nutrients were consumed, although some bacteria died during experiments. The model accurately predicted pressure behavior during shut-in periods, aligning with experimental data.

Chisholm et al. [7] carried out an investigation on microbial-enhanced oil recovery. The three-phase study showed that residual oil saturation can be reduced by introducing gas in a water wet system. The decrease in the interfacial tension was achieved as a result of metabolic products.

Devi et al. [8] studied the effect of a three-dimensional hybrid Cu-Al_2O_3/water nanofluid flow over a sheet with a Lorentz force and Newtonian heating. They used similarity transformations to convert the governing PDEs to ODEs and solved them using the Nachtsheim–Swigert shooting iteration technique and the Runge–Kutta–Fehlberg integration method. The results showed that hybrid nanofluid had a higher heat transfer rate than other nanoparticles.

Guzei et al. [9] studied thermophysical properties of nanofluid in two-phase fluid flow through a porous rectangular medium for enhanced oil recovery. The study revealed that greater volume of oil maybe recovered by using nanofluid flooding. The results showed that adding nanoparticles to a base fluid enhanced the oil recovery. They also noted that increasing the inlet temperature enhanced oil recovery due to changes in the viscosity and density of oil.

Md Basir et al. [10] examined nanofluid slip flow over a cylinder, employing the Runge–Kutta–Fehlberg fourth-order numerical method within Maple 18 symbolic software. Their findings indicated that elevating the bioconvection Schmidt number led to a reduction in the density function of motile microorganisms.

Mehryan et al. [11] carried out a study on fluid flow and heat transfer analysis of a nanofluid over a stretching vertical surface. They used similarity transformation to convert the PDEs into ODEs. The arising equations were then discretized using the finite difference method and linearized by employing Newton's Linearization technique, and were then solved by the Thomas algorithm. The study showed that the density of the microorganisms increases with the increase in magnetic parameter.

Morel [12] investigated the hydrodynamic modelling of oil–water stratified smooth turbulent flow in horizontal circular pipes. They considered a two-dimensional numerical simulation by focusing on pressure gradient, flow-field and oil–water interface height. The finite volume method accurately predicted velocity field of the pipeline cross section, which is helpful for controlling flow assurance issues, such as wax deposition, hydrate formation and pipeline corrosion.

Muhammad et al. [13] carried out a study on heat transfer analysis in the slip flow of hybrid nanomaterial with Newtonian heating. They carried out flow analysis by considering slip boundary and stagnation point. They considered Bvp4c to solve the model. They noticed that the Nusselt number shows the best performance in terms of increasing in the presence of hybrid nanomaterial. The study considered heat transport through Newtonian heating and thermal radiation. The study was aimed at enhancing the efficiency of the industry by basically improving heat transport rate and reducing surface friction coefficient.

Mutuku & Makinde [14] carried out research on the hydro-

magnetic bioconvection of nanofluid over a vertical plate due to microorganisms. They incorporated both Brownian motion and thermophoresis effects in the model. The equations were solved using appropriate similarity transformation and shooting quadrature coupled with a Runge–Kutta–Fehberg integration scheme. The heating as a result of viscous dissipation and nanoparticles interaction aggravated by Brownian motion and thermophoresis reduces the viscosity of the fluid, hence increasing its mobility.

Nima et al. [15] studied the melting effect on non-Newtonian fluid flow in gyro-tactic microorganism-saturated non-Darcy porous media with variable fluid properties. The governing equations were transformed using a similarity transformation and solved using Bvp4c. The results indicated that velocity profiles decreased while the temperature rose for mixed convection and decreased for melting.

Raees et al. [16] investigated mixed convection in gravity-driven nano-liquid film containing both nanoparticles and gyro-tactic microorganisms. They used the Buongiorno model to come up with the model and solved the resulting equations using the finite difference technique. They noted that bioconvection in nanofluids has great potential in enhancing mass and heat transport, mixing and improving the stability of nanofluids.

Shaw et al. [17] carried out an investigation into the magnetic field and viscous dissipation effect on bioconvection in a permeable sphere embedded in a porous medium with a nanofluid containing gyro-tactic microorganisms. The results showed that the introduction of magnetic fields in the system decreases the skin friction, local nanoparticle Sherwood number and local density of microorganisms.

Zhang et al. [18] examined the impact of magnetic Reynolds number on the swimming behavior of gyro-tactic microorganisms between rotating circular plates filled with nanofluids. They used Pade approximation to solve the resulting differential equations and found that increasing the thermophoresis parameter raised temperature. The Peclet number reduced microorganism density, while the Schmidt number increased it.

Hussaini et al. [19] examined the effects of various factors on unsteady viscoelastic periodic flow through a porous medium channel under specific conditions, including the presence of slip conditions, radiation, and constant heat and mass flux. The governing non-linear partial differential equations were solved using the perturbation method. The findings indicated that the diffusive thermo effect enhances velocity while reducing skin friction, particularly for larger values. The angle of inclination and heat source parameter also contribute to increased velocity, although the viscoelastic parameter reduces it.

Sharma &Prabhakar [20] explored the numerical simulation of the generalized FitzHugh-Nagumo equation using the shifted Chebyshev spectral collocation method. This approach employed shifted Chebyshev polynomials to approximate the spatial variable and its derivatives, while Chebyshev-Gauss-Lobatto points were used for the collocation process. By applying this method, the FitzHugh-Nagumo equation were transformed into a system of nonlinear ordinary differential equations, which were then solved using the fourth-order Runge-Kutta scheme. The numerical solutions obtained were presented in both graphical and tabular formats, illustrating the convergence of the method. A comparison with exact and approximate solutions derived from other methods reveals that this method provides improved accuracy, underscoring its effectiveness in solving such equations.

Buzuzi et al. [21] carried out a numerical investigation of the influence of the effective Prandtl number on the steady magnetohydrodynamic Williamson nanofluid flow over an inclined stretching surface, taking into account the effects of an aligned magnetic field, heat generation, and chemical reactions. The equations were solved numerically using the MATLAB software package, specifically utilizing the boundary value problem solver. The findings revealed that an increase in the effective Prandtl number reduces the concentration profile near the wall, along with the temperature and velocity profiles. The velocity is observed to be highest when both the slope of the channel and the inclination angle of the magnetic field are at their lowest.

Buzuzi et al. [22] conducted a numerical analysis of steady magnetohydrodynamic convective flow in a viscous, incompressible, electrically conducting fluid over an inclined stretching surface. The partial differential equations governing the flow were converted into a system of nonlinear ordinary differential equations, which were then solved numerically using the MATLAB software package. The findings suggested that to achieve an optimal velocity profile, both the inclination of the magnetic field and the stretching surface should be minimized. Furthermore, for a given effective Prandtl number, the Prandtl number should exceed the radiation parameter to enhance the flow properties.

Nithya & Vennila [23] examined how thermal radiation and the presence of heat sources or sinks affect the flow of a hybrid nanofluid composed of aluminum oxide and titanium dioxide nanoparticles dispersed in water. The governing equations are solved using the bvp4c algorithm, and the influence of different parameters on velocity and temperature is analyzed through graphical results. The findings indicate that an increase in the magnetic parameter raises the temperature and influences the velocity distribution.

Buzuzi [24] examined how channel slope, magnetic field alignment, and effective Prandtl number influence the flow of a magnetohydrodynamic Maxwell fluid with heat generation and thermophoresis. They found that a higher effective Prandtl number raises the fluid's temperature and concentration but lowers its velocity. The fluid's concentration peaks when the channel slope and magnetic field angle are both minimal or both maximal, depending on the Prandtl number. The temperature is highest with a maximum channel slope and minimal magnetic field angle. Increasing the thermophoretic parameter reduces skin friction and mass transfer but improves heat transfer.

The novelty of this study is to break new ground by adopting a comprehensive approach to modeling multiphase flow in oil recovery, addressing complexities often neglected in previous research such as; integrating elements like hybrid gyro-tactic nanofluids, microorganisms, suction and injection, variable viscosity and thermal conductivity, and thermal radiation. The consideration of a convergent pipe domain adds realism to the model, while the consideration of flow unsteadiness bridges the gap between theory and real-world conditions, offering valuable insights for engineers tackling

oil recovery challenges. This consideration was not considered by the previous researchers.

II. Mathematical Formulation

This research analyzes the flow dynamics in a porous convergent pipe. It focuses on a stratified two-layer flow scenario, featuring an incompressible fluid and gyro-tactic microorganisms through an inclined pipe, as shown in Figure 1. The oil phase is placed at the upper half of the pipe, while the water phase is at the bottom. The fluid flow is laminar and unsteady. Viscosity is a non-linear function of temperature and is in a tangential direction in both phases. The source of energy for the fluid flow is viscous dissipation, thermal radiation and chemical reaction. Thermal conductivity changes with temperature.

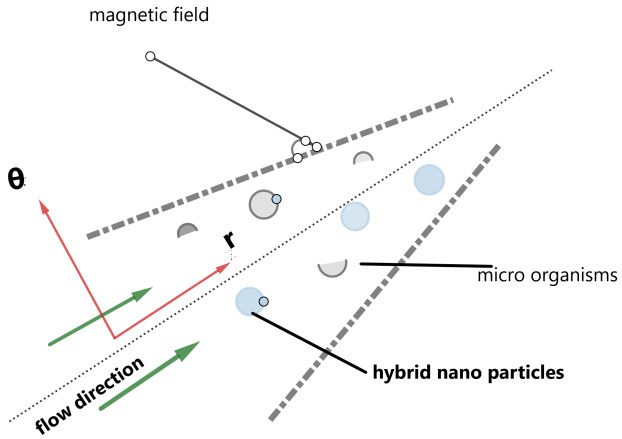

Fig. 1. Flow Geometry

This study adopts the assumption of laminar flow, treating the fluid as incompressible. Additionally, it considers an unsteady flow regime and a constant magnetic field.

A. The effective properties of hybrid nanofluid

The hybrid nanofluid considered in this study is Cu-Al_2O_3-H_2O/OIL. We adopt the pseudo-single-phase methodology in which the composite two-phase amalgamation of water and oil is regarded as a unified fluidic entity. The characteristic attributes of this pseudofluid are ascertained by averaging pertinent physical properties associated with water and oil. The dynamic viscosity, density, heat capacity, thermal expansion coefficient, thermal conductivity and electrical conductivity, as used by many researchers such as (Othman et al.) [25], are given, respectively, as follows:

$$\mu_{hnf} = \mu_f(1-\phi_1)^{-2.5}(1-\phi_2)^{-2.5} \tag{1}$$

$$\frac{\rho_{hnf}}{\rho_f} = (1-\phi_2)\left[(1-\phi_1)+\phi_1\frac{\rho_1}{\rho_f}\right]+\phi_2\frac{\rho_2}{\rho_f} \tag{2}$$

$$\frac{(\rho C_p)_{hnf}}{(\rho C_p)_f} = (1-\phi_2)\left[(1-\phi_1)+\phi_1\frac{(\rho C_p)_1}{(\rho C_p)_f}\right]+\phi_2\frac{(\rho C_p)_2}{(\rho C_p)_f} \tag{3}$$

$$\frac{(\rho\beta)_{hnf}}{(\rho\beta)_f} = (1-\phi_2)\left[(1-\phi_1)+\phi_1\frac{(\rho\beta)_1}{(\rho\beta)_f}\right]+\phi_2\frac{(\rho\beta)_2}{(\rho\beta)_f} \tag{4}$$

$$\frac{k_{hnf}}{k_{bf}} = \frac{k_2+2k_{bf}-2\phi_2(k_{bf}-k_2)}{k_2+2k_{bf}+\phi_2(k_{bf}-k_2)} \tag{5}$$

$$\frac{k_{bf}}{k_f} = \frac{k_1+2k_f-2\phi_1(k_f-k_1)}{k_1+2k_f+\phi_1(k_f-k_1)} \tag{6}$$

$$\frac{\sigma_{hnf}}{\sigma_{bf}} = \frac{\sigma_2+2\sigma_{bf}-2\phi_2(\sigma_{bf}-\sigma_2)}{\sigma_2+2\sigma_{bf}+\phi_2(\sigma_{bf}-\sigma_2)} \tag{7}$$

$$\frac{\sigma_{bf}}{\sigma_f} = \frac{\sigma_1+2\sigma_f-2\phi_1(\sigma_f-\sigma_1)}{\sigma_1+2\sigma_f+\phi_1(\sigma_f-\sigma_1)} \tag{8}$$

where the subscript 1 represents the Al_2O_3 component and subscript 2 represents Cu solid component, hnf symbolize hybrid nanofluid, bf symbolize base fluid and f symbolize the fluid.

The thermophysical properties of density, heat capacity, thermal conductivity, viscosity, electrical conductivity and thermal expansion are provided as documented in (Akhavan-Behabadi et al.) [26] in Table I.

TABLE I
Thermophysical Properties

Physical Properties	ρ (Kg/m^3)2	C_p (J/KgK)	K (W/mK)	σ (S/m)	$\beta \times 10^{-5}$
Al_2O_3	3970	765	40	1.0×10^{-10}	0.65
Cu	8933	385	401	58×10^6	1.67
H_2O	997.1	4184	0.613	0.055	20.7
Crude Oil	881	2300	0.2	1.0×10^{-9}	120

III. Governing Equations

The equations that govern the flow of oil, water, hybrid nanoparticles and microorganisms include the equations of continuity, conservation of momentum, energy, concentration and the density of microorganisms. The equation of continuity is given as (Mehryan et al.) [11]

$$\frac{\partial}{\partial r}(ru_r) = 0 \tag{9}$$

The equation of continuity shows that the fluid flow is possible.

The equation of conservation of momentum is given as (Mehryan et al.) [11]

$$\rho_{hnf}\left(\frac{\partial u_r}{\partial t}+u_r\frac{\partial u_r}{\partial r}+\frac{u_\theta}{r}\frac{\partial u_r}{\partial \theta}-\frac{u_\theta^2}{r}\right) = -\frac{\partial p}{\partial r} + \left(\frac{1}{r}\frac{\partial}{\partial r}(r\tau_{rr})+\frac{1}{r}\frac{\partial}{\partial\theta}(r\tau_{\theta r})-\frac{\tau_{\theta\theta}}{r}\right)+\rho_{hnf}\vec{F}_r \tag{10}$$

$$\rho_{hnf}\left(\frac{\partial u_\theta}{\partial t}+u_r\frac{\partial u_\theta}{\partial r}+\frac{u_\theta}{r}\frac{\partial u_\theta}{\partial\theta}+\frac{u_r u_\theta}{r}+u_z\frac{\partial u_\theta}{\partial z}\right) = -\frac{1}{r}\frac{\partial p}{\partial\theta}+\left(\frac{1}{r^2}\frac{\partial}{\partial r}\left(r^2\tau_{r\theta}\right)+\frac{1}{r}\frac{\partial}{\partial\theta}(\tau_{\theta\theta})\right) + \frac{\partial}{\partial z}(\tau_{z\theta})+\frac{\tau_{\theta r}-\tau_{r\theta}}{r}+\rho_{hnf}\vec{F}_\theta \tag{11}$$

The shear stress is a function of the velocity gradient, that is

$$\tau = \mu_{hnf}\left[\vec{\nabla}\vec{u}+(\vec{\nabla}\vec{u})^T\right]-\frac{2}{3}\mu_{hnf}(\vec{\nabla}\cdot\vec{u})\delta_{ij} \tag{12}$$

Where δ_{ij} is the kronecker delta function defined as

$$\delta_{ij} = \begin{cases} 1 & \text{if } i=j \\ 0 & \text{if } i\neq j \end{cases} \tag{13}$$

In cylindrical coordinate system

$$\vec{\nabla}\vec{u} = \{e_r\frac{\partial}{\partial r}+e_\theta\frac{1}{r}\frac{\partial}{\partial\theta}+e_z\frac{\partial}{\partial z}\}\{e_r u_r+e_\theta u_\theta+e_z u_z\} \tag{14}$$

$$\vec{\nabla}\vec{u}+\left(\vec{\nabla}\vec{u}\right)^T-\frac{2}{3}\left(\vec{\nabla}\cdot\vec{u}\right) = \begin{bmatrix} 2\frac{\partial u_r}{\partial r}-\frac{2}{3}\left(\vec{\nabla}\cdot\vec{u}\right) & \frac{\partial u_\theta}{\partial r}+\left(\frac{1}{r}\frac{\partial u_r}{\partial\theta}-\frac{u_\theta}{r}\right) & \frac{\partial u_z}{\partial r}+\frac{\partial u_r}{\partial z} \\ \left(\frac{1}{r}\frac{\partial u_r}{\partial\theta}-\frac{u_\theta}{r}\right)+\frac{\partial u_\theta}{\partial r} & 2\left(\frac{1}{r}\frac{\partial u_\theta}{\partial\theta}+\frac{u_r}{r}\right)-\frac{2}{3}\left(\vec{\nabla}\cdot\vec{u}\right) & \frac{\partial u_z}{\partial\theta}+\frac{\partial u_\theta}{\partial z} \\ \frac{\partial u_z}{\partial z}+\frac{\partial u_z}{\partial r} & \frac{\partial u_\theta}{\partial z}+\frac{\partial u_z}{\partial\theta} & 2\frac{\partial u_z}{\partial z}-\frac{2}{3}\left(\vec{\nabla}\cdot\vec{u}\right) \end{bmatrix} \tag{15}$$

Using the condition that the velocity u_θ is constant suction/injection and the flow is two dimensional in radial and θ directions, the shear stress components are given as

$$\tau_{rr} = 2\mu_{hnf}\frac{\partial u_r}{\partial r}, \tau_{r\theta} = \mu_{hnf}\left[\frac{\partial u_\theta}{\partial r}+\left(\frac{1}{r}\frac{\partial u_r}{\partial\theta}-\frac{u_\theta}{r}\right)\right] \tag{16}$$

$$\tau_{\theta\theta} = \mu_{hnf}\left[2\left(\frac{1}{r}\frac{\partial u_\theta}{\partial\theta} + \frac{u_r}{r}\right)\right] \quad (17)$$

$$\tau_{\theta r} = \mu_{hnf}\left[\frac{\partial u_\theta}{\partial r} + \left(\frac{1}{r}\frac{\partial u_r}{\partial\theta} - \frac{u_\theta}{r}\right)\right] \quad (18)$$

A. Buoyancy Forces

The buoyancy forces in the flow are influenced by temperature differences, concentration gradients, and variations in microorganism density. These factors affect the fluid's density universally, impacting flow dynamics broadly rather than solely in buoyancy calculations. The density is given as

$$\rho_{hnf} = \rho_{\infty_{hnf}} + \left(\frac{\partial\rho_{hnf}}{\partial T}\right)_p (T - T_\infty) + \left(\frac{\partial\rho_{hnf}}{\partial C}\right)_p (C - C_\infty) \quad (19)$$

$$+ \left(\frac{\partial\rho_{hnf}}{\partial N}\right)_p (N - N_\infty) \quad (20)$$

Therefore, buoyancy force in the r-direction is given by

$$F_r = \rho_{hnf} g \sin\beta_1[\beta_T(T - T_\infty) + \beta_C(C - C_\infty) + \beta_N(N - N_\infty)] \quad (21)$$

The buoyancy force in the θ direction is given as

$$F_\theta = \rho_{hnf} g \cos\beta_1[\beta_T(T - T_\infty) + \beta_C(C - C_\infty) + \beta_N(N - N_\infty)] \quad (22)$$

Substituting (18),(17), (21) and (22) in (10) and (11), we have

$$\rho_{hnf}\left(\frac{\partial u_r}{\partial t} + u_r\frac{\partial u_r}{\partial r}\right) = -\frac{\partial p}{\partial r} + \left(\frac{1}{r}\frac{\partial}{\partial r}\left(2r\mu_{hnf}\frac{\partial u_r}{\partial r}\right)\right) + \left[\frac{1}{r}\frac{\partial}{\partial\theta}\left(r\mu_{hnf}\left[\left(\frac{1}{r}\frac{\partial u_r}{\partial\theta}\right)\right]\right) - \mu_{hnf}\left[2\left(\frac{u_r}{r}\right)\right]\right] + \rho_{hnf}\left[g\beta_T(T - T_\infty)\sin\beta_1 + g\beta_C(C - C_\infty)\sin\beta_1\right] + \rho_{hnf}\left[g\beta_N(N - N_\infty)\sin\beta_1\right] + \rho_{hnf}\vec{F_r} \quad (23)$$

Equation (23) is the equation of conservation of momentum in the radial direction.

$$\rho_{hnf}\left(\frac{u_r u_\theta}{r}\right) = -\frac{1}{r}\frac{\partial p}{\partial\theta} + \frac{1}{r^2}\frac{\partial}{\partial r}\left(r^2\mu_{hnf}\left[\left(\frac{1}{r}\frac{\partial u_r}{\partial\theta} - \frac{u_\theta}{r}\right)\right]\right) + \frac{1}{r}\frac{\partial}{\partial\theta}\left(\mu_{hnf}\left[2\frac{u_r}{r}\right]\right) + \rho_{hnf}\left[g\beta_T(T - T_\infty)\cos\beta_1\right] + \rho_{hnf}\left[g\beta_C(C - C_\infty)\cos\beta_1 + g\beta_N(N - N_\infty)\cos\beta_1 + \vec{F_\theta}\right] \quad (24)$$

Equation (24) is the equation of conservation of momentum in the θ direction

Ampere's law combines Ampere's circuital law with Maxwell's addition to account for the displacement current. It is mathematically expressed as $\vec{\nabla}\times\vec{B} = \mu_0\vec{J} + \mu_0\epsilon_0\frac{\partial\vec{E}}{\partial t}$. The first term $(\mu_0\vec{J})$ represents the magnetic field $\vec{B}$ produced by the electric current density $\vec{J}$. The second term $(\mu_0\epsilon_0\frac{\partial\vec{E}}{\partial t})$ describes how a time-varying electric field can also produce a magnetic field.

From Ohm's law, $\vec{J} = \sigma_{hnf}(\vec{E} + \vec{V}\times\vec{B})$. The total electromagnetic force also known as Lorentz force is given by $\vec{J}\times\vec{B}$, since there is no externally applied electric field; thus, $\vec{E}$ is negligible.

The inclined magnetic field components are given as $(B_r, B_\theta, B_z) = (B_0\cos\alpha, B_0\sin\alpha, 0)$

So,

$$\vec{J} = \sigma_{hnf}(\vec{V}\times\vec{B}) = \sigma_{hnf}\begin{vmatrix}\hat{r} & \hat{\theta} & \hat{k}\\ u_r & 0 & 0\\ B_0\cos\alpha & B_0\sin\alpha & 0\end{vmatrix} \quad (25)$$

$$J = \sigma_{hnf}B_0 u_r\sin\alpha\hat{k} \quad (26)$$

The cumulative electromotive force is therefore given as

$$\vec{J}\times\vec{B} = \begin{vmatrix}\hat{r} & \hat{\theta} & \hat{k}\\ 0 & 0 & \sigma_{hnf}B_0 u_r\sin\alpha\\ B_0\cos\alpha & B_0\sin\alpha & 0\end{vmatrix} \quad (27)$$

$$\vec{j}\times\vec{B} = (-\sigma_{hnf}B_0^2 u_r\sin^2\alpha)\vec{r} + (\sigma_{hnf}B_0^2 u_r\cos\alpha\sin\alpha)\hat{\theta} \quad (28)$$

Substituting the Lorentz force Equation (28) into Equations (23) and (24), the equations in the radial and θ directions are given, respectively, as

$$\rho_{hnf}\left(\frac{\partial u_r}{\partial t} + u_r\frac{\partial u_r}{\partial r} + \frac{u_\theta}{r}\frac{\partial u_r}{\partial\theta} - \frac{u_\theta^2}{r}\right) = -\frac{\partial p}{\partial r} + \frac{1}{r}\frac{\partial}{\partial r}\left(2r\mu_{hnf}\frac{\partial u_r}{\partial r}\right) + \frac{1}{r}\frac{\partial}{\partial\theta}\left(r\mu_{hnf}\left[\frac{1}{r}\frac{\partial u_r}{\partial\theta} - \frac{u_\theta}{r}\right]\right) - \mu_{hnf}\left[2\frac{u_r}{r^2}\right] + \rho_{hnf}\left[g\beta_T(T - T_\infty)\sin\beta_1 + g\beta_C(C - C_\infty)\sin\beta_1\right] + \rho_{hnf}\left[g\beta_N(N - N_\infty)\sin\beta_1\right] - \rho_{hnf}\sigma_{hnf}B_0^2 u_r\sin^2\alpha + \rho_{hnf}\vec{F_r} \quad (29)$$

$$\rho_{hnf}\left(\frac{u_r u_\theta}{r}\right) = -\frac{1}{r}\frac{\partial p}{\partial\theta} + \frac{1}{r^2}\frac{\partial}{\partial r}\left(r^2\mu_{hnf}\left[\frac{1}{r}\frac{\partial u_r}{\partial\theta} - \frac{u_\theta}{r}\right]\right) + \frac{1}{r}\frac{\partial}{\partial\theta}\left(\mu_{hnf}\left[2\left(\frac{1}{r}\frac{\partial u_\theta}{\partial\theta} + \frac{u_r}{r}\right)\right]\right) + \rho_{hnf}\left[g\beta_T(T - T_\infty)\cos\beta_1\right] + \rho_{hnf}\left[g\beta_C(C - C_\infty)\cos\beta_1\right] + \rho_{hnf}\left[g\beta_N(N - N_\infty)\cos\beta_1\right] + \rho_{hnf}\sigma_{hnf}B_0^2 u_r\cos\alpha\sin\alpha + \rho_{hnf}\vec{F_\theta} \quad (30)$$

According to (Chisholm et al.) [7], permeability is part of the proportionality constant in Darcy's law, which relates discharge and fluid physical properties to a pressure gradient applied to the porous media.

Darcy's law describes the flow of fluids through a porous medium and states that the velocity of fluid flow through the porous material between two points is directly proportional to the pressure gradient $(\frac{dp}{dr})$ and inversely proportional to both the fluid's viscosity (μ_{hnf}) and the distance (or length) between the two points. Thus,

$$u_r = \frac{-k}{\mu_{hnf}}\left(\frac{dp}{dr}\right) \quad (31)$$

For a flow in a gravitational field, Darcy's law may be generalized to

$$-\frac{dp}{dr} = \frac{\mu_{hnf}}{k}u_r + \frac{c_k}{k^{\frac{1}{2}}}\rho_{hnf}u_r^2 \quad (32)$$

c_k is the Forchheimer constant, which is usually determined experimentally for different porous media.

The linear Darcy's term describing the distributed body force extended by the fibers in the porous medium is retained, but the nonlinear Forchheimer term is neglected.

$$-\Delta p + \frac{\mu_{hnf}}{k}\vec{u} = 0 \quad (33)$$

Substituting (33) into (29) and differentiating partially with respect to θ, we have

$$0 = -\frac{1}{\rho_{hnf}}\frac{\partial^2 p}{\partial r\partial\theta} + \frac{1}{\rho_{hnf}}\frac{\partial\mu_{hnf}}{\partial\theta}\left[\frac{2}{r}\frac{\partial u_r}{\partial r} + \frac{2}{r}\frac{\partial^2 u_r}{\partial r^2} + \frac{2}{r}\frac{\partial^2 u_r}{\partial\theta^2}\right] - \frac{1}{\rho_{hnf}}\frac{\partial\mu_{hnf}}{\partial\theta}\left[\frac{1}{r}\frac{\partial u_\theta}{\partial\theta} - \frac{2}{r^2}u_r - \frac{1}{k}u_r\right] + \frac{1}{r\rho_{hnf}} \times \left[\frac{\partial^2\mu_{hnf}}{\partial\theta^2}\frac{\partial u_r}{\partial\theta} - u_\theta\frac{\partial^2\mu_{hnf}}{\partial\theta^2}\right] + \frac{\mu_{hnf}}{\rho_{hnf}}\left[\frac{2}{r}\frac{\partial^2 u_r}{\partial r\partial\theta} + 2\frac{\partial^3 u_r}{\partial r^2\partial\theta}\right] + \frac{\mu_{hnf}}{\rho_{hnf}}\left[\frac{1}{r}\frac{\partial^3 u_r}{\partial\theta^3} - \frac{2}{r^2}\frac{\partial u_r}{\partial\theta} - \frac{1}{k}\frac{\partial u_r}{\partial\theta}\right] - \frac{\partial^2 u_r}{\partial t\partial\theta} - \frac{\partial u_r}{\partial\theta}\frac{\partial u_r}{\partial r} - u_r\frac{\partial^2 u_r}{\partial r\partial\theta} - \frac{u_\theta}{r}\frac{\partial^2 u_r}{\partial\theta^2} + g\sin\beta_1\left[\beta_T\frac{\partial}{\partial\theta}(T - T_\infty)\right] + g\sin\beta_1\left[\beta_C\frac{\partial}{\partial\theta}(C - C_\infty)\right] - g\sin\beta_1\left[\beta_N\frac{\partial}{\partial\theta}(N - N_\infty)\right] - \sigma_{hnf}B_0^2\sin^2\alpha\frac{\partial u_r}{\partial\theta} \quad (34)$$

Substituting (33) into (30) and differentiating partially with respect to r, we have

$$0 = \frac{1}{\rho_{hnf}}\frac{\partial^2 p}{\partial\theta\partial r} + \frac{1}{\rho_{hnf}}\frac{\partial\mu_{hnf}}{\partial\theta}\left[-\frac{2}{r}\frac{\partial u_r}{\partial r}\right] + \frac{1}{r\rho_{hnf}} \times \left[-2u_r\frac{\partial^2\mu_{hnf}}{\partial\theta\partial r}\right] + \frac{\mu_{hnf}}{\rho_{hnf}}\left[\frac{3}{r^2}\frac{\partial u_r}{\partial\theta} - \frac{3}{r}\frac{\partial^2 u_r}{\partial\theta\partial r} - \frac{\partial^3 u_r}{\partial r^2\partial\theta}\right] + \frac{\mu_{hnf}}{\rho_{hnf}}\left[-\frac{u_\theta}{r^2} + \frac{u_\theta}{k}\right] - \frac{2u_r}{r^2\rho_{hnf}}\frac{\partial\mu_{hnf}}{\partial\theta} - g\cos\beta_1 \times \left[\beta_T(T-T_\infty) + r\beta_T\frac{\partial}{\partial r}(T-T_\infty) + \beta_C(C-C_\infty)\right] - g\cos\beta_1\left[r\beta_C\frac{\partial}{\partial r}(C-C_\infty) + \beta_N(N-N_\infty)\right] - g\cos\beta_1\left[r\beta_N\frac{\partial}{\partial r}(N-N_\infty)\right] - B_0^2 u_r\cos\alpha\sin\alpha - rB_0^2\cos\alpha\sin\alpha\frac{\partial u_r}{\partial r} + u_\theta\frac{\partial u_r}{\partial r} \quad (35)$$

Adding the equations (34) and (35) and considering the thermo-physical properties equations (1) to (8), to obtain,

$$\frac{B}{G}\frac{1}{\rho_f}\frac{\partial\mu_f}{\partial\theta}\left[\frac{2}{r}\frac{\partial^2 u_r}{\partial r^2} + \frac{2}{r}\frac{\partial^2 u_r}{\partial\theta^2} - \frac{1}{r}\frac{\partial u_\theta}{\partial\theta} - \frac{2}{r^2}u_r - \frac{1}{k}u_r\right] + \frac{B}{rG\rho_f}\left[\frac{\partial^2\mu_f}{\partial\theta^2}\frac{\partial u_r}{\partial\theta} - u_\theta\frac{\partial^2\mu_f}{\partial\theta^2} - 2u_r\frac{\partial^2\mu_f}{\partial\theta\partial r}\right] + \frac{\mu_f}{\rho_f}A \times \left[\frac{\partial^3 u_r}{\partial r^2\partial\theta} + \frac{1}{r}\frac{\partial^3 u_r}{\partial\theta^3} - \frac{1}{k}\frac{\partial u_r}{\partial\theta} + \frac{1}{r^2}\frac{\partial u_r}{\partial\theta} - \frac{1}{r}\frac{\partial^2 u_r}{\partial\theta\partial r}\right] + \frac{\mu_f}{\rho_f}A \times \left[-\frac{u_\theta}{r^2} + \frac{u_\theta}{k}\right] - \frac{\partial^2 u_r}{\partial t\partial\theta} - \frac{\partial u_r}{\partial\theta}\frac{\partial u_r}{\partial r} - u_r\frac{\partial^2 u_r}{\partial r\partial\theta} - \frac{u_\theta}{r}\frac{\partial^2 u_r}{\partial\theta^2} + u_\theta\frac{\partial u_r}{\partial r} + g\sin\beta_1\left[\beta_T\frac{\partial}{\partial\theta}(T-T_\infty) + \beta_C\frac{\partial}{\partial\theta}(C-C_\infty)\right] + g\sin\beta_1\left[\beta_N\frac{\partial}{\partial\theta}(N-N_\infty)\right] - g\cos\beta_1\left[\beta_T(T-T_\infty)\right] + r\beta_T\frac{\partial}{\partial r}(T-T_\infty) - g\cos\beta_1\left[\beta_C(C-C_\infty) + r\beta_C\frac{\partial}{\partial r}(C-C_\infty)\right] - g\cos\beta_1\left[\beta_N(N-N_\infty) + r\beta_N\frac{\partial}{\partial r}(N-N_\infty)\right] - \sigma_f F B_0^2 \times \sin^2\alpha\frac{\partial u_r}{\partial\theta} - B_0^2 u_r\cos\alpha\sin\alpha - rB_0^2\cos\alpha\sin\alpha\frac{\partial u_r}{\partial r} = 0 \quad (36)$$

The fluid considered is non-Newtonian, the power law model for viscosity is given by $\mu_f = \mu_0 g^{n-1}$, where g is the velocity gradient, since g is a function of θ alone, then

$$\frac{\partial\mu_f}{\partial\theta} = (n-1)\mu_0 g^{n-2}g' \quad (37)$$

and

$$\frac{\partial^2\mu_f}{\partial^2\theta} = \mu_0(n-1)\left[(n-2)g^{n-3}(g')^2 + g^{n-2}g''\right] \quad (38)$$

Substituting the equations (37) and (38) in the equation (36), we have

$$\left[\mu_0(n-1)\{(n-2)g^{n-3}(g')^2 + g^{n-2}g''\}\right]\frac{B}{G} \times \left[\frac{1}{r\rho_f}\frac{\partial u_r}{\partial\theta} - \frac{u_\theta}{r\rho_f}\right] + \left[\frac{(n-1)\mu_0 g^{n-2}g'}{\rho_f}\right]\frac{B}{G} \times \left[\frac{2}{r}\frac{\partial^2 u_r}{\partial r^2} + \frac{1}{r}\frac{\partial^2 u_r}{\partial\theta^2} - \frac{2}{r^2}u_r - \frac{u_r}{k} - \frac{2u_r}{r^2}\right] + \frac{\mu_0 g^{n-1}}{\rho_f}A\left[\frac{\partial^3 u_r}{\partial r^2\partial\theta} + \frac{1}{r}\frac{\partial^3 u_r}{\partial\theta^3} - \frac{1}{k}\frac{\partial u_r}{\partial\theta} + \frac{1}{r^2}\frac{\partial u_r}{\partial\theta}\right] - \frac{\mu_0 g^{n-1}}{\rho_f}A\left[\frac{1}{r}\frac{\partial^2 u_r}{\partial\theta\partial r} - \frac{u_\theta}{r^2} + \frac{1}{k}u_\theta\right] - \frac{\partial^2 u_r}{\partial t\partial\theta} - \frac{\partial u_r}{\partial\theta}\frac{\partial u_r}{\partial r} - u_r\frac{\partial^2 u_r}{\partial r\partial\theta} - \frac{u_\theta}{r}\frac{\partial^2 u_r}{\partial\theta^2} + u_\theta\frac{\partial u_r}{\partial r} + g\sin\beta_1\left[\beta_T\frac{\partial}{\partial\theta}(T-T_\infty)\right] + g\sin\beta_1\left[\beta_C\frac{\partial}{\partial\theta}(C-C_\infty) + \beta_N\frac{\partial}{\partial\theta}(N-N_\infty)\right] - g\cos\beta_1\left[\beta_T(T-T_\infty) + r\beta_T\frac{\partial}{\partial r}(T-T_\infty) + \beta_C(C-C_\infty)\right] - g\cos\beta_1\left[r\beta_C\frac{\partial}{\partial r}(C-C_\infty) + \beta_N(N-N_\infty)\right] - g\cos\beta_1\left[r\beta_N\frac{\partial}{\partial r}(N-N_\infty)\right] - \sigma_f F B_0^2\sin^2\alpha\frac{\partial u_r}{\partial\theta} - B_0^2 u_r\cos\alpha\sin\alpha - rB_0^2\cos\alpha\sin\alpha\frac{\partial u_r}{\partial r} = 0 \quad (39)$$

From the assumptions given and considering viscous dissipation, Joule heating, and thermal radiation, the equation of energy becomes (Devi) [11]

$$(\rho C_p)_{hnf}\left[\frac{\partial T}{\partial t} + u_r\frac{\partial T}{\partial r} + u_\theta\frac{\partial T}{\partial\theta}\right] = \frac{1}{r}\frac{\partial}{\partial r}\left(k_{hnf}r\frac{\partial T}{\partial r}\right) + \frac{1}{r}\frac{\partial}{\partial\theta}\left(\frac{k_{hnf}}{r}\frac{\partial T}{\partial\theta}\right) + \mu_{hnf}\left[2\left(\frac{\partial u_r}{\partial r}\right)^2 + 2\left(\frac{u_r}{r}\right)^2\right] + \mu_{hnf}\left[\left(-\frac{u_\theta}{r} + \frac{1}{r}\frac{\partial u_r}{\partial\theta}\right)^2\right] + \frac{\vec{J}^2}{\sigma_{hnf}} - \frac{1}{r}\frac{\partial q_r}{\partial\theta} \quad (40)$$

The joule heating is the heat produced as a result of resistance as electric current passes through a conductor. From Ohms law,

$$\vec{J} = \sigma_{hnf}(\vec{E} + \vec{V}\times\vec{B}) \quad (41)$$

since there is no externally applied electric field, $\vec{E}$

Given that;

$$(\vec{V}\times\vec{B}) = \begin{vmatrix} \hat{r} & \hat{\theta} & \hat{z} \\ u_r & 0 & 0 \\ B_0\cos\alpha & B_0\sin\alpha & 0 \end{vmatrix} \quad (42)$$

$$\frac{\vec{J}^2}{\sigma_{hnf}} = \sigma_{hnf}\left[\vec{V}\times\vec{B})\right]\cdot\left[\vec{V}\times\vec{B})\right] \quad (43)$$

$$\frac{\vec{J}^2}{\sigma_{hnf}} = \sigma_{hnf}u_r^2 B_0^2\sin^2\alpha \quad (44)$$

Substituting (44) in equation (40), it becomes

$$(\rho C_p)_{hnf}\left[\frac{\partial T}{\partial t} + u_r\frac{\partial T}{\partial r} + u_\theta\frac{\partial T}{\partial\theta}\right] = \frac{1}{r}\frac{\partial}{\partial r}\left(k_{hnf}r\frac{\partial T}{\partial r}\right) + \frac{1}{r}\frac{\partial}{\partial\theta}\left(\frac{k_{hnf}}{r}\frac{\partial T}{\partial\theta}\right) + \mu_{hnf}\left[2\left(\frac{\partial u_r}{\partial r}\right)^2 + 2\left(\frac{u_r}{r}\right)^2\right] + \mu_{hnf}\left[\left(-\frac{u_\theta}{r} + \frac{1}{r}\frac{\partial u_r}{\partial\theta}\right)^2\right] + \sigma_{hnf}u_r^2 B_0^2\sin^2\alpha - \frac{1}{r}\frac{\partial q_r}{\partial\theta} \quad (45)$$

In equation (45) q_r is the thermal radiation. (Mukhopadhyay) [27] described $q_r = \frac{-4\sigma^*}{3k^* r}\frac{\partial T^4}{\partial\theta}$, where σ^* is the Stefan-Boltzman constant, k^* is the absorption co-efficient. The quadratic thermal radiation aspect is appropriate in the situations where the quadratic variation of temperature is accounted for in the thermal convection. It is worth noting that q_r can not be negative, its the temperature

difference that is negative, that is the temperature gradient is from the region of high to low temperature.

T^4 is expanded using Taylor's series as a linear function, the difference between the temperature at the wall and the free stream is small. Hence,

$$T^4 \approx 4T_\infty^3 T - 3T_\infty^4 \tag{46}$$

Using this expression in Rosselands approximation q_r, we have;

$$q_r = -\frac{4\sigma^*}{3k^*}\frac{1}{r}\frac{\partial}{\partial\theta}\left[4T_\infty^3 T - 3T_\infty^4\right] = -\frac{16\sigma^*}{3k^* r}T_\infty^3\frac{\partial T}{\partial\theta} \tag{47}$$

Substitution (47) in the equation (45) and using the fact that variable thermal conductivity is a function of temperature we have,

$$\begin{aligned}\frac{\partial T}{\partial t} + u_r\frac{\partial T}{\partial r} + u_\theta\frac{\partial T}{\partial\theta} = \frac{k^*_{hnf}}{(\rho C_p)_{hnf}}\frac{b}{\Delta T}\left(\frac{\partial T}{\partial r}\right)^2 + \frac{k^*_{hnf}}{(\rho C_p)_{hnf}} \\ \times\left[1 + b\frac{T-T_\infty}{\Delta T}\right]\left(\frac{1}{r}\frac{\partial T}{\partial r} + \frac{\partial^2 T}{\partial r^2} + \frac{1}{r^2}\frac{\partial^2 T}{\partial\theta^2}\right) \\ + \frac{k^*_{hnf}}{(\rho C_p)_{hnf} r^2}\frac{b}{\Delta T}\left(\frac{\partial T}{\partial\theta}\right)^2 + \frac{\mu_{hnf}}{(\rho C_p)_{hnf}}\left[2\left(\frac{\partial u_r}{\partial r}\right)^2 + 2\left(\frac{u_r}{r}\right)^2\right] \\ + \frac{\mu_{hnf}}{(\rho C_p)_{hnf}}\left[\left(\frac{u_\theta}{r}\right)^2 - \frac{2u_\theta}{r^2}\frac{\partial u_r}{\partial\theta} + \frac{1}{r^2}\left(\frac{\partial u_r}{\partial\theta}\right)^2\right] \\ + \frac{\sigma_{hnf}}{(\rho C_p)_{hnf}}u_r^2 B_0^2\sin^2\alpha + \frac{1}{(\rho C_p)_{hnf}}\frac{16\sigma^* T_\infty^3}{3k^* r^2}\frac{\partial^2 T}{\partial\theta^2}\end{aligned} \tag{48}$$

Under the given assumptions and incorporating thermophoresis velocity, the equation of concentration becomes (Devi) [11]

$$\begin{aligned}\frac{\partial C}{\partial t} + u_r\frac{\partial C}{\partial r} + \frac{u_\theta}{r}\frac{\partial C}{\partial\theta} = D_{hnf}\left[\frac{1}{r}\frac{\partial C}{\partial r} + \frac{\partial^2 C}{\partial r^2} + \frac{1}{r^2}\frac{\partial^2 C}{\partial\theta^2}\right] \\ - \frac{k_1\mu_{hnf}}{\rho_{hnf} r^2}\left[-\frac{C}{T^2}\left(\frac{\partial T}{\partial\theta}\right)^2 + \frac{C}{T}\frac{\partial^2 T}{\partial\theta^2} + \frac{1}{T}\frac{\partial T}{\partial\theta}\frac{\partial C}{\partial\theta}\right] \\ - \frac{k_1 C}{\rho_{hnf} T r^2}\frac{\partial\mu_{hnf}}{\partial\theta}\frac{\partial T}{\partial\theta} - K_r C\end{aligned} \tag{49}$$

The behavior of microorganisms is governed by a complex set of equations that take into account a variety of factors, including their concentration within a given fluid. The equation of microorganism density is given by (Devi) [11]

$$\frac{\partial N}{\partial t} + u_r\frac{\partial N}{\partial r} + \frac{u_\theta}{r}\frac{\partial N}{\partial\theta} + \frac{dw_c}{(c-c_\infty)}\left[\frac{1}{r}\frac{\partial N}{\partial\theta}\frac{\partial C}{\partial\theta} + \frac{N}{r}\frac{\partial^2 C}{\partial\theta^2}\right] = D_m\left[\frac{1}{r^2}\frac{\partial^2 N}{\partial\theta^2}\right] \tag{50}$$

In order to solve the nonlinear partial differential equation that governs multiphase flow, it is necessary to have the suitable boundary conditions.

In the case of a two-phase stratified oil-water flow, the boundary conditions includes specifications for both the oil-water interface and the pipe wall. The wall of the pipe, as well as the oil-water interface, adhere to a no-slip condition. The temperature and velocity at the outlet are assumed to be fully developed, with zero temperature and velocity gradients in the radial direction.

At the pipe wall, $\theta = \pm\alpha$

$$u_r = 0, u_\theta = u_o, T = T_w, C = C_w, N = N_w \tag{51}$$

At $\theta = 0$, the interface is treated as a moving wall.

$$u_r = u_\infty, u_\theta = 0, T = T_\infty, C = C_\infty, N = N_\infty \tag{52}$$

At $r = 0$

$$u_r = u_\infty, u_\theta = 0, T = T_\infty, C = C_\infty, N = N_\infty \tag{53}$$

At $r = \infty$, the gradients of all variables in the flow direction are zero as proposed by (Mavi and Chinyoka) [28].

$$\frac{\partial u_\theta}{\partial r} = 0, \frac{\partial u_r}{\partial r} = 0, \frac{\partial T}{\partial r} = 0, \frac{\partial C}{\partial r} = 0, \frac{\partial N}{\partial r} = 0 \tag{54}$$

It is a requirement that the equations (39), (48), (49) and (50) are transformed into ordinary differential equation using similarity transformation before solving them numerically by Spectral method.

Ojiambo et al. [29] defined the unsteady boundary layer equation, which is based on time dependent length scale as

$$u(x,t) = \frac{\nu x^m}{\delta^{m+1}} \tag{55}$$

Where ν represents the kinematic viscosity, δ is a time dependent length scale, m is an arbitrary constant that is related to the wedge angle and x is the distance across the pipe.

Nagler [30] defined the velocity of two dimensional steady boundary layer is $u_r = -\frac{Qf(\theta)}{r}$, where Q represents the planar volumetric flow rate.

Since the flow is unsteady, we have

$$u_r(\theta,t) = -\frac{Q}{r}\frac{1}{\delta^{m+1}}f(\theta) \tag{56}$$

It is a requirement that the transformation is made dimensionless by using the transformation $\eta = \frac{\theta}{\alpha}$.

Hence,

$$u_r(\theta,t) = -\frac{Q}{r}\frac{1}{\delta^{m+1}}f(\eta) \tag{57}$$

The transformation for equation of conservation of energy, concentration of species and micro organisms density equations were done using.

$$\frac{\omega(\eta)}{\delta^{m+1}} = \frac{T-T_w}{T_\infty - T_w} \tag{58}$$

$$\frac{\phi(\eta)}{\delta^{m+1}} = \frac{C-C_w}{C_\infty - C_w} \tag{59}$$

$$\frac{\Theta(\eta)}{\delta^{m+1}} = \frac{N-N_w}{N_\infty - N_w} \tag{60}$$

It is a requirement that the similarity transform given by equation (57) should certisfy the equation of continuity (49) that is

$$\frac{\partial}{\partial r}(ru_r) = 0 \tag{61}$$

$$\left(\frac{Q}{r}\frac{1}{\delta^{m+1}}f\right) - \left(\frac{Q}{r}\frac{1}{\delta^{m+1}}f\right) = 0 \tag{62}$$

Hence it satisfies the equation of continuity showing that its an appropriate transformation.

By applying the similarity transformations as defined in equations (57) in the equation (39), to obtain,

$$\begin{aligned}\left[(n-1)\{(n-2)g^{n-3}(g')^2 + g^{n-2}g''\}\right]\frac{B}{G} \\ \times\left[-r^2 f' - \frac{r^3}{Q}\delta^{m+1}u_\theta\right] + \left[(n-1)g^{n-2}g'\right]\frac{B}{G} \\ \times\left[-4f - r^2 f'' + 4rf + \frac{r^3}{k}f\right] + g^{n-1}A \\ \times\left[-4rf' - r^2 f''' + \frac{r^3}{k}f' - \frac{r^2}{Q}u_\theta\delta^{m+1} + \frac{r^4 u_\theta\delta^{m+1}}{Qk}\right] \\ - \frac{\rho_f(m+1)r^3}{\mu_0\delta}\frac{d\delta}{dt}f' + \frac{2Qr\rho_f}{\mu_0\delta^{m+1}}ff' + \frac{\rho_f}{\mu_0}u_\theta r^2 f'' + \frac{\rho_f}{\mu_0}r^2 u_\theta f \\ + \frac{g\rho_f r^4\sin\beta_1}{\mu_0 Q}\left[\beta_T(T_\infty - T_w)\omega' + \beta_C(C_\infty - C_w)\phi'\right] \\ + \frac{g\rho_f r^4\sin\beta_1}{\mu_0 Q}\left[\beta_N(N_\infty - N_w)\Theta' - \beta_T(T_\infty - T_w)\omega\right] \\ - \frac{g\rho_f r^4\cos\beta_1}{\mu_0 Q}\left[\beta_C(C_\infty - C_w)\phi + \beta_N(N_\infty - N_w)\Theta\right] \\ + \left(\frac{\sigma_f F B_0^2 r^3\rho_f\sin^2\alpha}{\mu_0}\right)f' = 0\end{aligned} \tag{63}$$

The following dimensionless parameters arise from the model, $Re = \frac{ru_\theta}{\nu_f} = \frac{Q}{\nu_f r}$, $Gr_{(T)} = \frac{gr^3\beta_T(T_\infty - T_w)}{\nu_f}$, $Gr_{(C)} = \frac{gr^3\beta_C(C_\infty - C_w)}{\nu_f}$,$Gr_{(N)} = \frac{gr^3\beta_N(N_\infty - N_w)}{\nu_f}$, $Ha = B_0 r\sqrt{\frac{\sigma_f}{\mu_f}}$, $\lambda = \frac{\delta^m \rho_f}{\mu_f r^{m-1}}\frac{d\delta}{dt}$ and $Da = \frac{kQ}{ru_\theta}$. Using the dimensionless numbers in the equation (63), simplifying and using the assumption that the viscosity is a function of tangential direction, $\mu_{hnf} = \mu_0 g^{n-1}$ and $g = g(\theta) = \theta^s$ for $s \neq 0$ (Nagler) [30], to obtain,

$$
\begin{aligned}
&[s(n-1)\{s(n-1)-1\}]\,\theta^{s(n-1)-2}\frac{B}{G}\left[-r^2 f' - \frac{r^3}{Q}\delta^{m+1}u_\theta\right] \\
&+\left[s(n-1)\theta^{s(n-1)-1}\right]\frac{B}{G}\left[-4f - r^2 f'' + 4rf + \frac{r^3}{k}f\right] \\
&+\theta^{s(n-1)}A\left[-4rf' - r^2 f''' + \frac{r^3}{k}f' - \frac{r^2}{Q}u_\theta\delta^{m+1} + \frac{r^3\delta^{m+1}}{Da}\right] \\
&-(m+1)\frac{r^{m+2}}{\delta^{m+1}}\lambda f' + \frac{2r^2}{\delta^{m+1}}Ref f' + rRef'' + rRef \\
&+\frac{r}{Q}\sin\beta_1\left[Gr_{(T)}\omega' + Gr_{(C)}\phi' + Gr_{(N)}\Theta'\right] - \frac{r}{Q}\cos\beta_1 \\
&\times\left[Gr_{(T)}\omega + Gr_{(C)}\phi + Gr_{(N)}\Theta\right] + Ha^2 F(r\sin^2\alpha)f' = 0
\end{aligned}
\tag{64}
$$

Substituting the similarity transformation (58) into the equation (48) and simplifying, to obtain

$$
\begin{aligned}
&\left[\frac{k^*_{hnf}}{(C_p)_{hnf}\mu_{hnf}} + \frac{k^*_{hnf}}{(C_p)_{hnf}\mu_{hnf}}b.\frac{T_\infty - T_w}{\Delta T} + \right]\omega'' \\
&+\left[\frac{16\sigma^* T_\infty^3}{3k^*(C_p)_{hnf}\mu_{hnf}}\right]\omega'' + \frac{k^*_{hnf}}{(C_p)_{hnf}\mu_{hnf}}.\frac{b(T_\infty - T_w)}{\Delta T\delta^{m+1}}(\omega')^2 \\
&-u_\theta\frac{\rho_{hnf}}{\mu_{hnf}}r^2\omega' + \frac{m+1}{\sigma}\frac{\rho_{hnf}}{\mu_{hnf}}r^2\frac{d\delta}{dt}\omega + \frac{Q^2}{(T_\infty - T_w)(C_p)_{hnf}} \\
&\times\left[\frac{4}{r^2\delta^{m+1}}f^2 + \frac{\delta^{m+1}(u_\theta)^2}{Q^2}\right] + \frac{Q^2}{(T_\infty - T_w)(C_p)_{hnf}} \\
&\times\left[\frac{2u_\theta}{rQ}f' + \frac{1}{r^2\delta^{m+1}}(f')^2\right] \\
&+\frac{\sigma_{hnf}}{\delta^{m+1}}\frac{Q^2 B_0^2\sin^2\alpha}{(T_\infty - T_w)(C_p)_{hnf}\mu_{hnf}}f^2 = 0
\end{aligned}
\tag{65}
$$

From the thermophysical properties, equations (1) to (8), to obtain

$$
\begin{aligned}
&\left[\frac{k^*_f}{(C_p)_f\mu_f}\frac{C}{DB} + \frac{k^*_f}{(C_p)_f\mu_f}b.\frac{T_\infty - T_w}{\Delta T}\frac{C}{DB}\right. \\
&\left.+\frac{16\sigma^* T_\infty^3}{3k^*(C_p)_f\mu_f DB}\right]\omega'' + \frac{k^*_f}{(C_p)_f\mu_f}\frac{C}{DB}.\frac{b(T_\infty - T_w)}{\Delta T\delta^{m+1}}(\omega')^2 \\
&-u_\theta\frac{\rho_f}{\mu_f}\frac{1}{A}r^2\omega' + \frac{m+1}{\sigma}\frac{\rho_f}{\mu_f}\frac{1}{A}r^2\frac{d\delta}{dt}\omega + \frac{Q^2}{(T_\infty - T_w)(C_p)_f D} \\
&\times\left[\frac{4}{r^2\delta^{m+1}}f^2 + \frac{\delta^{m+1}(u_\theta)^2}{Q^2}\right] + \frac{Q^2}{(T_\infty - T_w)(C_p)_f D} \\
&\times\left[\frac{2u_\theta}{rQ}f' + \frac{1}{r^2\delta^{m+1}}(f')^2\right] \\
&+\frac{\sigma_f}{\delta^{m+1}}\frac{Q^2 B_0^2\sin^2\alpha}{(T_\infty - T_w)(C_p)_f\mu_f}\frac{F}{DB}f^2 = 0
\end{aligned}
\tag{66}
$$

Factoring in the following dimensionless numbers , $Pr = \frac{\mu_f(C_p)_f}{k^*_f}$, $R = \frac{16\sigma^* T_\infty^3}{3k^*}$, $\lambda = \frac{\delta^m\rho_f}{\mu_f r^{m-1}}\frac{d\delta}{dt}$, $Ec = \frac{Q^2}{(C_p)_f(T_\infty - T_w)}$, $Re = \frac{ru_\theta}{\nu_f}$ and $J = \frac{\sigma_f B_0^2\sin^2\alpha}{\rho_f(C_p)_f\nu_f(T_\infty - T_w)}$ into the equation (66), to obtain

$$
\begin{aligned}
&\frac{1}{DB\ Pr}\left[C + C\ b + \frac{R}{k_f C}\right]\omega'' + \frac{1}{Pr}\frac{bC}{DB}\frac{1}{\delta^{m+1}}(\omega')^2 \\
&-\frac{r}{A}Re\omega' + \frac{(m+1)}{A}\frac{r^{m+1}}{\delta^{m+1}}\lambda\omega + \frac{Ec}{D}\left[\frac{4}{r^2\delta^{m+1}}f^2 + \delta^{m+1}\frac{u_\theta^2}{Q^2}\right] \\
&+\frac{Ec}{D}\left[\frac{2u_\theta}{rQ}f' + \frac{1}{r^2\delta^{m+1}}(f')^2\right] + \frac{F}{DB}\frac{Q^2}{\delta^{m+1}}Jf^2 = 0
\end{aligned}
\tag{67}
$$

Substituting the equations (1) to (8) in (49),

$$
\begin{aligned}
&(m+1)\frac{\rho_f r^2}{\mu_f\delta}\frac{1}{A}\frac{d\delta}{dt}\phi - \frac{\rho_f u_\theta r}{\mu_f}\frac{1}{A}\phi' + D_{hnf}\frac{\rho_f}{\mu_f}\frac{1}{A}\phi'' \\
&+k_1\left(\frac{C_w\delta^{m+1}}{(C_\infty - C_w)} + \phi\right)\left(\frac{1}{\frac{T_w\delta^{m+1}}{(T_\infty - T_w)} + \omega)}\right)\left(\frac{1}{\frac{T_w\delta^{m+1}}{(T_\infty - T_w)} + \omega}\right) \\
&\times(\omega')^2 - k_1\left(\frac{C_w}{C_\infty - C_w} + \phi\right)\left(\frac{1}{\frac{T_w}{T_\infty - T_w} + \omega}\right)\omega'' \\
&+\left(\frac{1}{\frac{(T_w\delta^{m+1}}{(T_\infty - T_w} + \omega}\right)(\omega'\phi') - k_1\left(\frac{C_w\delta^{m+1}}{C_\infty - C_w} + \phi\right)\left(B\frac{\partial\mu_f}{\partial\theta}\right) \\
&\times\left(\frac{1}{\frac{T_w\delta^{m+1}}{T_\infty - T_w} + \omega}\omega'\right) - \frac{k_r\rho_f r^2}{\mu_f}\frac{1}{A}\left(\frac{C_w\delta^{m+1}}{C_\infty - C_w} + \phi\right) = 0
\end{aligned}
\tag{68}
$$

The non-dimensional numbers defined here are $\lambda = \frac{\delta^m}{\mu_f}\frac{\rho_f}{r^{m-1}}\frac{d\delta}{dt}$, $Sc = \frac{\nu_f}{D_f}$, $Re = \frac{ru_\theta}{\nu_f}$, $Nt = \frac{T_w}{T_\infty - T_w}$, $Nc = \frac{C_w}{C_\infty - C_w}$ and $Kc = \frac{k_r\nu_f}{u_\theta}$.
Substituting the dimensionless parameters in the equation (68), to obtain

$$
\begin{aligned}
&\frac{1}{A\ Sc}\phi'' - \frac{Re}{A}\phi' + \frac{(m+1)}{A}\frac{r^{m+1}}{\delta^{m+1}}\lambda\phi - \frac{k_1}{Nt\delta^{m+1} + \omega} \\
&\times\left[-\left(\frac{Nc\delta^{m+1} + \phi}{Nt\delta^{m+1} + \omega)}\right)(\omega')^2\right] - \frac{k_1}{Nt\delta^{m+1} + \omega} \\
&\times\left[(Nc + \phi)\left(\frac{Nt\delta^{m+1} + \omega}{Nt + \omega}\right)\omega'' + \omega'\phi'\right] - \frac{k_1}{Nt\delta^{m+1} + \omega} \\
&\times\left(Nc\delta^{m+1} + \phi\right)\left(B\frac{\partial\mu_f}{\partial\theta}\right)(\omega') - \frac{Kc}{A}Re\left(Nc\delta^{m+1} + \phi\right) = 0
\end{aligned}
\tag{69}
$$

From assumption the assumption that the viscosity is a function of tangential direction, $\mu_{hnf} = \mu_0 g^{n-1}$ and $g = g(\theta) = \theta^s$ for $s \neq 0$ (Nagler) [30]. Then the equation (69) becomes,

$$
\begin{aligned}
&\frac{1}{A\ Sc}\phi'' - \frac{Re}{A}\phi' + \frac{(m+1)}{A}\frac{r^{m+1}}{\delta^{m+1}}\lambda\phi - \frac{k_1}{Nt\delta^{m+1} + \omega} \\
&\times\left[-\left(\frac{Nc\delta^{m+1} + \phi}{Nt\delta^{m+1} + \omega)}\right)(\omega')^2\right] - \frac{k_1}{Nt\delta^{m+1} + \omega} \\
&\times\left[(Nc + \phi)\left(\frac{Nt\delta^{m+1} + \omega}{Nt + \omega}\right)\omega'' + \omega'\phi'\right] - \frac{\mu_0 k_1}{Nt\delta^{m+1} + \omega} \\
&\times\left(Nc\delta^{m+1} + \phi\right)\left(B(n-1)s\theta^{s(n-1)-1}\right)(\omega') \\
&-\frac{Kc}{A}Re\left(Nc\delta^{m+1} + \phi\right) = 0
\end{aligned}
\tag{70}
$$

Substituting the equations (60) in equation (50), simplifying and adding the thermophysical properties given by equations (1) to (8), the equation (70), becomes

$$
\begin{aligned}
&-(m+1)\frac{\rho_f r^2}{\mu_f A\delta}\frac{d\delta}{dt}\Theta + u_\theta r\frac{\rho_f}{\mu_f\ A}\Theta' + \frac{rdWc}{\mu_f B}\frac{1}{\delta^{m+1}}\Theta'\phi' \\
&+\frac{rdWc\rho_f}{A\ \mu_f}\left(\frac{N_w\delta^{m+1}}{N_\infty - N_w} + \Theta\right)\frac{1}{\delta^{m+1}}\phi'' = D_m\left[\frac{\rho_f}{A\ \mu_f}\Theta''\right]
\end{aligned}
\tag{71}
$$

The dimensionless parameters featured here are, $\lambda = \frac{\delta^m\rho_f}{\mu_f r^{m-1}}\frac{d\delta}{dt}$, $Re = \frac{ru_\theta}{\nu_f}$, $Pe = \frac{dWc}{D_m}$, $Lb = \frac{\nu_f}{D_m}$ and $Nn = \frac{N_w}{N_\infty - N_w}$.
Substituting the above dimensionless parameters into the equations (71), to obtain

$$\frac{Lb}{A}\Theta'' - \frac{Re}{A}\Theta' - \frac{Pe}{B\ Lb}r\Theta'\phi' + \frac{(m+1)}{A}\frac{r^{m+1}}{\delta^{m+1}}\lambda\Theta - \frac{rPe}{A\ Lb}\left(Nn\delta^{m+1} + \Theta\right)\frac{1}{\delta^{m+1}}\phi'' = 0 \quad (72)$$

Transforming the boundary conditions (51), (52),(53) and (54), using the transformations (57), (58), (59) and (60), to obtain
At $\theta = \pm\alpha$

$$f(\eta) = 0, \omega = 0, \phi = 0, \Theta = 0 \quad (73)$$

At $\theta = 0$

$$f(\eta) = -\frac{u_\infty r\delta^{m+1}}{Q}, f'(\eta) = 0, \omega = \delta^{m+1}, \phi = \delta^{m+1}, \Theta = \delta^{m+1} \quad (74)$$

At $r = 0$

$$f(\eta) = -\frac{u_\infty r\delta^{m+1}}{Q}, \omega = \delta^{m+1}, \phi = \delta^{m+1}, \Theta = \delta^{m+1} \quad (75)$$

At $r = \infty$

$$\frac{\partial f}{\partial r} = 0, \frac{\partial \omega}{\partial r} = 0, \frac{\partial \phi}{\partial r} = 0, \frac{\partial \Theta}{\partial r} = 0 \quad (76)$$

IV. Numerical Solution

The spectral relaxation method (SRM) is used to solve (64),(67), (70), and (76). The spectral relaxation method is a recent innovation that employs the Gauss–Seidel approach to decouple large systems of nonlinear equations.
The method assumes that solution of the differential equation takes the form

$$U(r) = \sum_{j=0}^{N} L_j(r_i)u_j \quad (77)$$

Where,

$$L_j(r) = \prod_{\substack{i=0 \\ i\neq j}}^{N} \frac{r - r_i}{r_j - r_i}, L_j(r_i) = \begin{cases} 1, i = j \\ 0, i \neq j \end{cases} \quad (78)$$

$L_j(r)$ are lagrange cardinal polynomials. The grid points used are the Chebyshev Gauss Lobatto points, that is the relative extremes of Chebyshev polynomial of first kind. This clustered grid points are not ill conditioned which to a greater extent improves the accuracy of the solution. They are given by;

$$\bar{r_i} = \cos\left(\frac{i\pi}{N}\right), i = 0, 1, 2, ..., N \quad (79)$$

defined over the interval $[-1, 1]$. There is need to apply linear transformation

$$r_i = \left(\frac{b-a}{2}\right)\bar{r_i} + \left(\frac{b+a}{2}\right) \quad (80)$$

that maps $\bar{r} \in [-1, 1]$ to the computational domain $[a, b]$.

The fundamental idea behind the spectral collocation method is the introduction of a differentiation matrix **D** which is used to approximate the derivative of the unknown variables at the collocation points as the matrix vector product.

The first derivative is approximated by;

$$U'(r) = \sum_{j=0}^{N} L_j'(r_i)u_j \sum_{j=0}^{N} L_j'(r_i)u_j = \sum_{j=0}^{N} D_{ij}u_j = \mathbf{DU}, \quad (81)$$

$$\mathbf{U''} = \mathbf{D}^2\mathbf{U}, \quad \mathbf{U'''} = \mathbf{D}^3\mathbf{U}, \quad \mathbf{U}^{(n)} = \mathbf{D}^n\mathbf{U}, n = 2, 3, 4... \quad (82)$$

The entries of Chebyshev differentiation matrix **D** are defined in (Trefethen) [31].

Spectral relaxation method(SRM) decouples linear terms at current iterative level. In addition, evaluate nonlinear terms at previous iteration level. The method is more accurate but converges slower than SQLM, and the rate of convergence is quadractic, just like the Newton Raphson method.

The SRM requires that an initial approximation to the solution is given. Starting from given initial approximations, the iteration schemes are solved for **U** which is inturn used to solve for **F**. In order to solve the equation, we discretize the equation using the chebyshev spectral method, before applying the spectral methods. In the spectral relaxation framework, we arrange the system of differential equations (64), (67), (70) and (76) as:

$$\begin{aligned} L_1[F, \omega, \Phi, \Theta] + N_1[F, \omega, \Phi, \Theta] = 0 \\ L_2[F, \omega, \Phi, \Theta] + N_2[F, \omega, \Phi, \Theta] = 0 \\ L_3[F, \omega, \Phi, \Theta] + N_3[F, \omega, \Phi, \Theta] = 0 \\ L_4[F, \omega, \Phi, \Theta] + N_4[F, \omega, \Phi, \Theta] = 0 \end{aligned} \quad (83)$$

where L stands for the linear differential operator and N stands for the non linear differential operator. Linear terms are evaluated at current iteration level $(r + 1)$, whereas Non-linear terms are evaluated at previous iterations (r).

$$\begin{aligned} L_1[F_{r+1}, \omega_r, \Phi_r, \Theta_r] + N_1[F_r, \omega_r, \Phi_r, \Theta_r] = 0 \\ L_2[F_{r+1}, \omega_{r+1}, \Phi_r, \Theta_r] + N_2[F_{r+1}, \omega_r, \Phi_r, \Theta_r] = 0 \\ L_3[F_{r+1}, \omega_{r+1}, \Phi_{r+1}, \Theta_r] + N_3[F_{r+1}, \omega_{r+1}, \Phi_r, \Theta_r] = 0 \\ L_4[F_{r+1}, \omega_{r+1}, \Phi_{r+1}, \Theta_{r+1}] + N_4[F_{r+1}, \omega_{r+1}, \Phi_{r+1}, \Theta_r] = 0 \end{aligned} \quad (84)$$

For the system of differential equations (64), (67), (70) and (76) the relaxation scheme is given as:

$$\begin{aligned} \left[-r^2A\theta^{s(n-1)}\right]f'''_{r+1} + \left[-r^2s(n-1)\theta^{s(n-1)-1}\frac{B}{G} + rRe\right] \\ \times f''_{r+1} + \left[-r^2s(n-1)\{s(n-1)-1\}e^{s(n-1)-2}\frac{B}{G}\right]f'_{r+1} \\ + \left[\theta^{s(n-1)}A\left(-4r + \frac{r^3}{k}\right)\right]f'_{r+1} - \left[(m+1)\frac{r^{m+2}}{\delta^{m+1}}\lambda\right]f'_{r+1} \\ + \left[Ha^2F(r\sin^2\alpha)\right]f'_{r+1} + [s(n-1)\theta^{s(n-1)-1}]\frac{B}{G}[-4] \\ + [s(n-1)\theta^{s(n-1)-1}]\frac{B}{G}\left[4r + \frac{r^3}{k} + rRe\right]f_{r+1} = \\ s(n-1)\{s(n-1)-1\}\theta^{s(n-1)-2}\frac{B}{G}\frac{r^3}{Q}\delta^{m+1}u_\theta \\ + \theta^{s(n-1)}A\left[\frac{r^2}{Q}u_\theta\delta^{m+1} - r^3\frac{\delta^{m+1}}{Da}\right] - \frac{2r^2}{\delta^{m+1}}Ref_rf'_r \\ - \frac{r}{Q}\sin\beta_1[G_{rT}\omega'_r + G_{rC}\Phi'_r + G_{rN}\Theta'_r] + \frac{r}{Q}\cos\beta_1 \\ \times [G_{rT}\omega_r + G_{rC}\Phi_r + G_{rN}\Theta_r] \end{aligned} \quad (85)$$

$$\begin{aligned} \frac{1}{DBPr}\left[c + c_b + \frac{R}{k_fc}\right]\omega''_{r+1} - \frac{r}{A}Re\omega'_{r+1} \\ + \frac{(m+1)}{A}\frac{r^{m+1}}{\delta^{m+1}}\lambda\omega_{r+1} = -\frac{1}{pr}\frac{bc}{DB}\frac{1}{\delta^{m+1}}(\omega'_r)^2 \\ - \frac{Ec}{D}\left[\frac{4}{r^2\delta^{m+1}}f_r^2 + \delta^{m+1}\frac{u_\theta^2}{Q^2} + \frac{2u_\theta}{rQ}f'_r + \frac{1}{r^2\delta^{m+1}}(f'_r)^2\right] \\ - \frac{F}{DB}\frac{Q^2}{\delta^{m+1}}J\ f_r^2 \end{aligned} \quad (86)$$

$$\frac{1}{A\ Sc}\Phi''_{r+1}+\left[-\frac{Re}{A}-\frac{k_1\omega'_{r+1}}{N_t\delta^{m+1}+\omega_{r+1}}\right]\Phi'_{r+1}$$
$$+\left[\frac{(m+1)}{A}\frac{r^{m+1}}{\delta^{m+1}}\lambda+\frac{k_1(\omega'_{r+1})^2}{(N_t\delta^{m+1}+\omega_{r+1})^2}-\frac{k_1\omega''_{r+1}}{N_t+\omega_{r+1}}\right]\Phi_{r+1}$$
$$+\left[\frac{-\mu_0 k_1}{N_t\delta^{m+1}+\omega_{r+1}}\left(B(n-1)s\theta^{s(n-1)-1}\right)\omega'_{r+1}-\frac{Kc}{A}Re\right]$$
$$\times\Phi_{r+1}=\frac{-k_1N_c\delta^{m+1}(\omega'_r)^2}{(N_t\delta^{m+1}+\omega_r)^2}+\frac{k_1N_c}{N_t+\omega_r}\omega''_r+\frac{\mu_0k_1}{N_t\delta^{m+1}+\omega_r}$$
$$\times N_c\delta^{m+1}\left[B(n-1)s\theta^{s(n-1)-1}\right]\omega'_r+\frac{k_c}{A}Re\left(N_c\delta^{m+1}\right) \quad (87)$$

$$\frac{Lb}{A}\Theta''_{r+1}+\left[-\frac{Re}{A}-\frac{Pe}{B\ Lb}r\Phi'_{r+1}\right]\Theta'_{r+1}$$
$$+\left[\frac{(m+1)r^{m+1}}{A\delta^{m+1}}\lambda-\frac{rPe}{A\ Lb\delta^{m+1}}\Phi''_{r+1}\right]\Theta_{r+1}=\frac{rPe}{ALb}Nn\Phi''_r \quad (88)$$

V. Computer Simulations

MATLAB software(R2020a) was used to obtain the flow profiles of the respective flow variables. The model requires the use of appropriate parameters, such as Pr for water and oil which are in the range of $5 < Pr < 7$ and $0 < Pr < 500$, respectively. Reynolds number are in the range of $0 \leq Re \leq 2000$ since we are dealing with laminar flow. The Eckert number 2.0 means that the flow kinetic energy is more than the enthalpy difference, $G_{rT} > 0$ represents the heating of the fluid which is in contact with the wall. The number of collocation points in the radial direction is taken as 50. The simulation yielded the results shown in the next section.

VI. Validation

The results of this study have been validated by comparing the fluid temperature profiles with those reported in the previous work by (Khan et al.) [32]. As depicted in Figure 10, the temperature profiles from both studies exhibit a strong agreement, particularly in their trends over time. This consistency in the results across different studies underscores the robustness and reliability of the model used in this research. The close match between the temperature profiles not only confirms the accuracy of the present model but also reinforces its applicability in simulating similar fluid dynamics scenarios.

VII. Results and Discussion

The Equations (85)–(88) were implemented in MATLAB and the results obtained in the form of graphs, which are discussed as follows.

A. Effects of Flow Parameters on Velocity

As shown in Figure 2, an increase in the Reynolds number leads to a rise in the velocity profiles. This is because a higher Reynolds number indicates a stronger influence of inertia forces compared to viscous forces. Inertia, the tendency of the fluid to maintain its motion, becomes more dominant, which increases the overall velocity. Conversely, viscous forces, which resist the fluid's motion, tend to retard the flow. However, as the Reynolds number increases, the impact of these viscous forces diminishes.

Since the flow under consideration is laminar, the fluid particles move smoothly in parallel layers with minimal mixing. The velocity profile reaches its maximum at a point just before the center of the pipe, where the influence of the adjacent immiscible fluid is most pronounced. As a result of this interaction, the fluid experiences a velocity drop due to the adjacent layer's effect. The no-slip condition on the walls of the pipes ensures that the fluid velocity gradually decreases to zero as it approaches the walls, reflecting the physical constraint that the fluid adheres to the boundary.

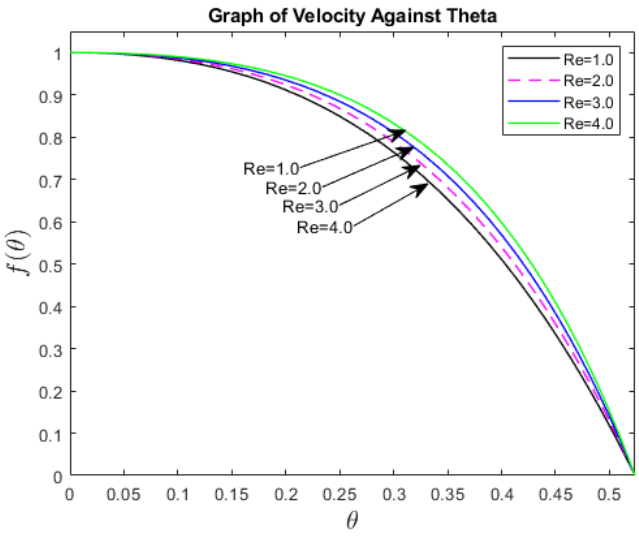

Fig. 2. Graph of velocity for varying Reynolds number.

As depicted in Figure 3, an increase in the thermal Grashof number results in an elevation of the velocity profiles. The thermal Grashof number quantifies the relative importance of buoyancy forces compared to viscous forces in the flow. As this number increases, it signifies that the buoyancy forces, driven by temperature differences, become more dominant than the viscous forces, which resist motion. This dominance of buoyancy forces enhances fluid motion, leading to an increase in fluid velocity.

The maximum velocity is observed at a point some distance away from the center of the pipe. This shift from the center is due to the influence of the boundary formed by the adjacent immiscible fluid, which alters the velocity distribution within the pipe. As the fluid approaches the pipe wall, the no-slip condition imposes that the velocity decreases gradually to zero, reflecting the adherence of the fluid to the wall and the resistance offered by the viscous forces at the boundary.

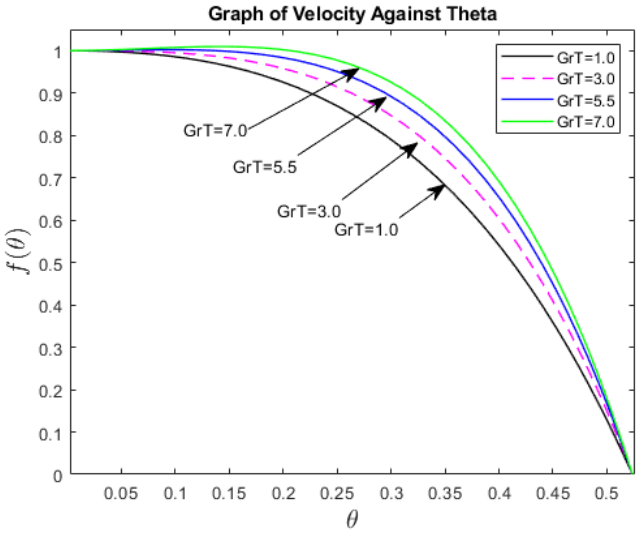

Fig. 3. Graph of velocity for varying thermal Grashof number.

Figure 4 illustrates that an increase in the microbial Grashof number results in a higher velocity of fluid flow. The microbial Grashof number reflects the influence of microbial activity on buoyancy forces relative to viscous forces. Microbial activity generates products like gases, which alter the fluid's density and viscosity. These changes in the density gradient enhance buoyancy-driven flow, leading to an increase in the velocity profile as the fluid moves in response to the varying densities.

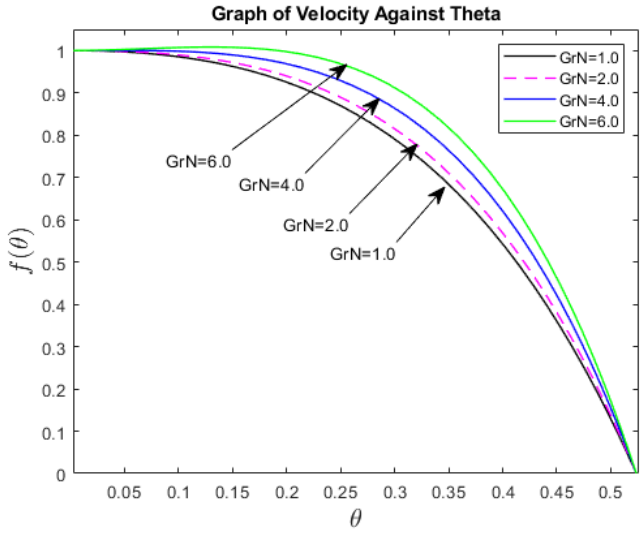

Fig. 4. Graph of velocity for varying microorganisms Grashof number.

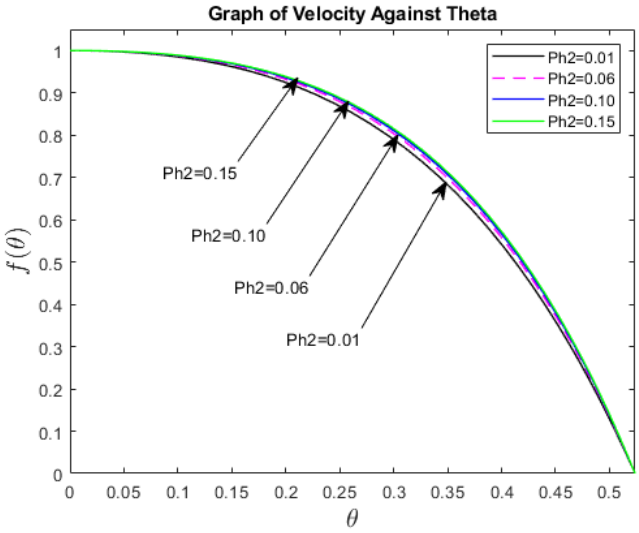

Fig. 6. Graph of Velocity for varying Volume fraction of Copper.

In addition, microorganisms exhibit chemotaxis, the ability to swim toward or away from chemical stimuli. This directed movement also contributes to the increase in fluid velocity as the collective motion of microorganisms amplifies the flow. Consequently, the combined effects of density changes due to microbial activity and chemotaxis lead to a significant increase in the velocity profiles within the fluid.

From figure (5) the observed decrease in the velocity profile with an increase in the volume fraction of aluminum oxide nanoparticles in a nanofluid. Addition of Aluminium oxide increases the fluid's viscosity, resulting in higher internal resistance to flow. The improved thermal conductivity of the nanofluid influences the momentum transfer, while the presence of nanoparticles leads to a thickening of the boundary layer near solid surfaces, further reducing the velocity.

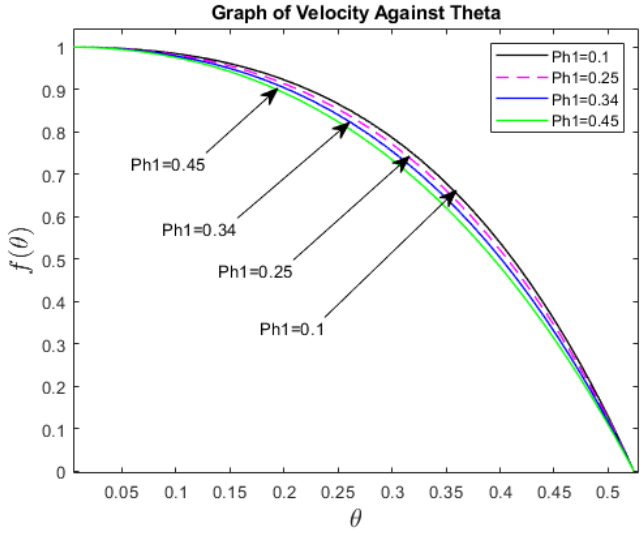

Fig. 5. Graph of Velocity for varying Volume fraction of Aluminium Oxide.

The increase in velocity profiles with rising copper nanoparticle volume fraction in a nanofluid as observed in figure (6) is because Copper has excellent thermal conductivity, which promotes higher flow velocities.

B. Effects of Flow Parameters on Temperature

Figure 7 shows that an increase in the Reynolds number leads to an increase in the temperature profiles. This occurs because a higher Reynolds number signifies an increase in the velocity of the fluid. As the fluid velocity increases, the friction between the fluid particles and the hybrid particles within the flow also intensifies. This increased interaction enhances heat transfer between fluid molecules, leading to an overall increase in temperature throughout the fluid.

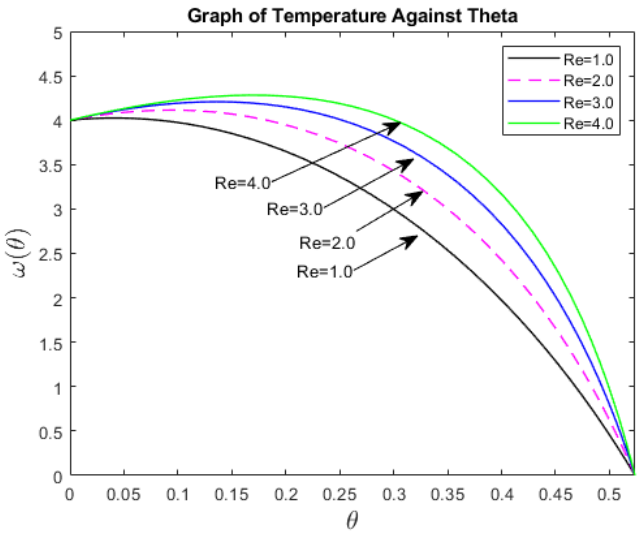

Fig. 7. Graph of temperature for varying Reynolds number.

The temperature reaches its maximum at a point just outside the center of the tube, where the combined effects of fluid velocity and particle interaction are most pronounced. As the fluid moves toward the wall of the pipe, the temperature gradually decreases. This decline reflects the reduced interaction near the boundary and the heat dissipation due to the cooler pipe walls.

From Figure 8, it is seen that an increase in the Eckert number leads to an increase in the temperature profiles, with a maximum value some distance from the center. An increase in the Ec number means an increase in the kinetic energy of the flow relative to the difference in enthalpy. This means that more kinetic energy promotes more vigorous mixing of the fluid. The vigorous mixing leads to the formation of heat energy as a result of the collisions of particles, leading to increased temperature profiles.

From Figure 9, an increase in the unsteadiness parameter (λ) leads to an increase in temperature profiles. An increase in the unsteadiness parameter means that the time derivatives in the governing equations become more significant compared to the

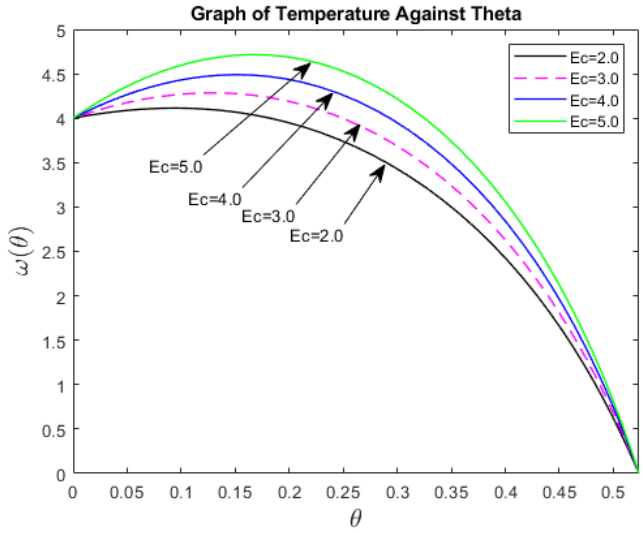

Fig. 8. Graph of temperature for varying Eckert number.

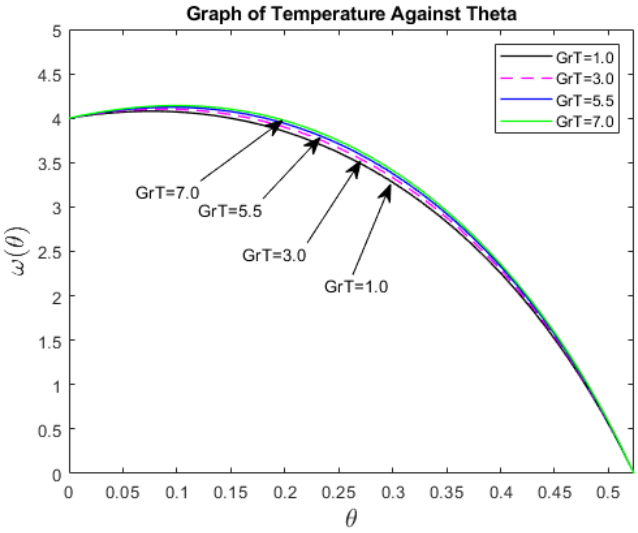

Fig. 10. Graph of temperature for varying thermal Grashof Number.

significant as compared to the spatial derivatives. This leads to faster changes in the temperature profiles over time.

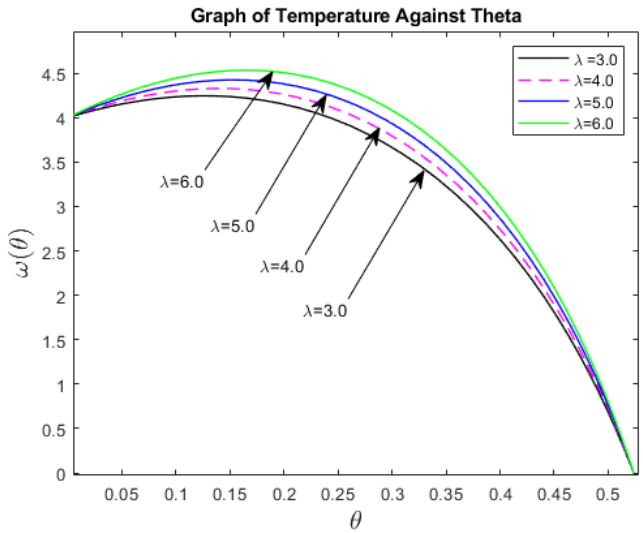

Fig. 9. Graph of temperature for varying Lambda number.

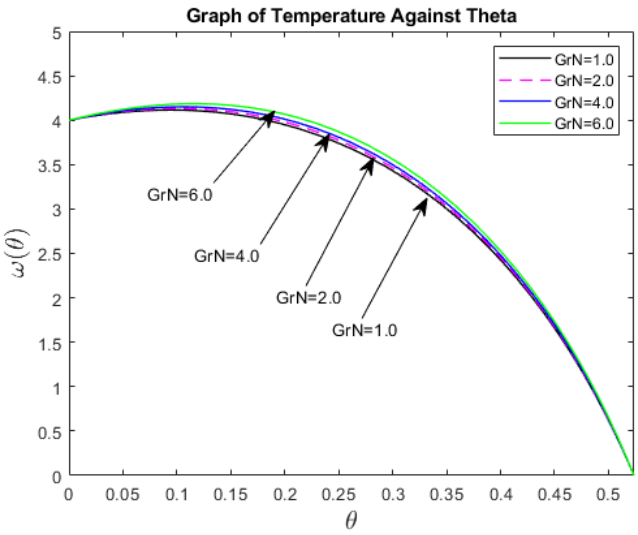

Fig. 11. Graph of temperature for varying microorganism Grashof number.

From Figure 10, it is seen that an increase in thermal Grashof number leads to an increase in temperature profiles. The thermal Grashof number, G_rT, is defined as the ratio of buoyancy forces to viscous forces. An increase in G_rT means that buoyancy forces dominate over viscous forces. This dominance enhances the fluid's natural tendency to move, resulting in stronger convection within the flow.

As G_rT increases, the fluid experiences more pronounced convection motion, which leads to more efficient heat transfer. This increased mixing within the fluid manifests as steeper temperature gradients or higher overall temperatures. The enhanced heat transfer, driven by the buoyancy-induced movement of the fluid, is reflected in the elevated temperature profiles as G_rT increases.

In Figure 11, an increase in G_rN leads to an increase in temperature profiles. The reason for the increase in temperature profiles is the interplay between microbial activity and fluid dynamics. Microorganisms are living organisms that metabolize and generate heat as a byproduct of their metabolic processes. This metabolic activity can lead to localized increases in temperature within their immediate surroundings. As G_rN increases, these localized temperature increases become more pronounced due to improved fluid motion and mixing.

Microorganisms often create gradients in nutrients concentration and metabolic byproducts in their environment. These gradients can drive fluid motion through processes such as chemotaxis (movement of microorganisms in response to chemical gradients) and bioconvection (movement induced by microorganism growth). As G_rN increases, buoyant forces become more dominant, leading to stronger fluid motion and enhanced mixing of temperature variations caused by microbial activity.

From Figure 12, it is observed that an increase in the radiation parameter leads to a decrease in temperature profiles. This occurs because a higher radiation parameter signifies that the material absorbs more radiation, leading to heat loss. Additionally, as the radiation parameter increases, the material becomes more reflective, further contributing to the reduction in temperature.

Moreover, some materials scatter incoming radiation rather than absorbing it. An increase in the radiation parameter, RR, enhances this scattering effect, making the absorption of radiation less effective and thereby resulting in lower temperatures within the material. This combination of increased heat loss, reflectivity, and scattering accounts for the observed decrease in temperature profiles as the radiation parameter increases.

From Figure 13, it is observed that an increase in the Joule heating parameter leads to an increase in the temperature profiles. When an electric current passes through a resistor, energy is

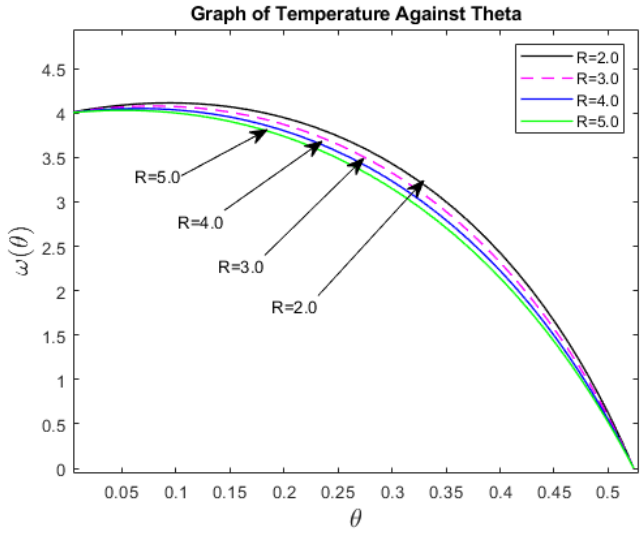

Fig. 12. Graph of temperature for varying Radiation parameter.

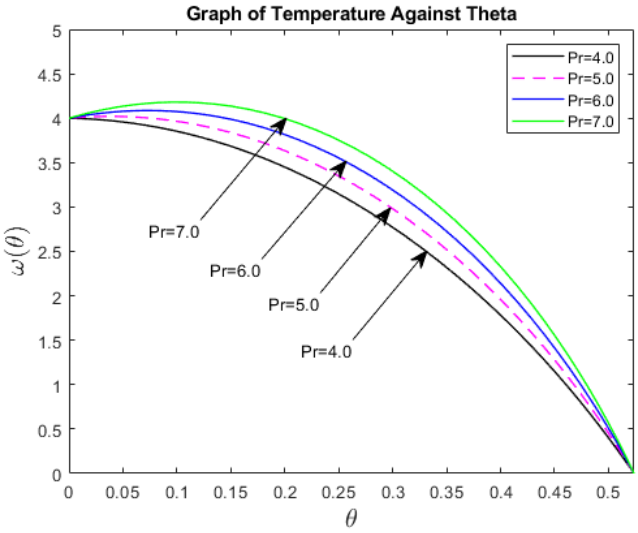

Fig. 14. Graph of temperature for varying Prandtl number.

dissipated in the form of heat because of the collisions between charge carriers and the atoms of the material. The amount of heat generated per unit time is directly proportional to the square of the current passing through the conductor and the resistance of the conductor. According to the first law of thermodynamics, energy cannot be created or destroyed, only transformed from one form to another. The induced current in the conductor is transformed into heat energy. The heat energy increases the internal energy of the material, leading to a rise in temperature. The temperature increases are proportional to the amount of heat generated, which in turn, is directly proportional to the Joule heating parameter.

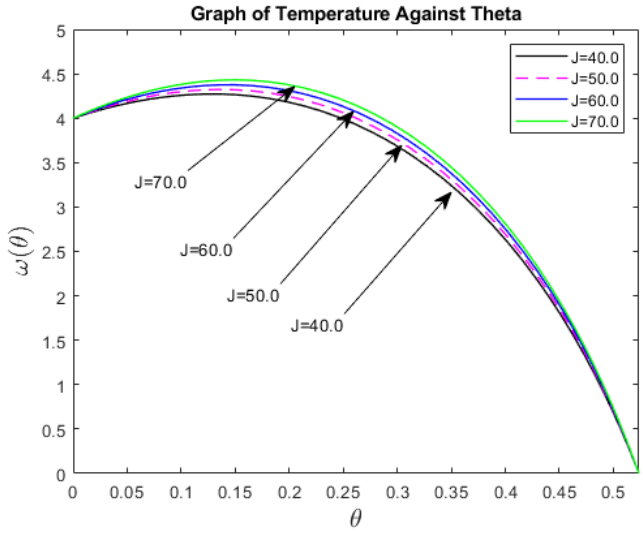

Fig. 13. Graph of temperature for varying Joule heating.

From Figure 14, it is observed that an increase in Prandtl number leads to an increase in the temperature profile. Pr is the ratio of momentum diffusivity to thermal diffusivity. It indicates how effectively momentum and heat are transported in a fluid. A higher Pr means that the thermal diffusivity is relatively lower compared to the momentum diffusivity. An increase in Pr leads to a thicker thermal boundary layer and a slower rate of heat transfer. Pr controls the relative thickness of the momentum and thermal boundary layers. This results in a more gradual temperature profile across the fluid, with the temperature gradient more evenly spread. Because momentum diffusivity is relatively higher compared to thermal diffusivity, there is more mixing within the fluid because momentum transport dominates over heat transport.

As observed in figure (15), the decrease in temperature profiles with an increasing volume fraction of aluminum oxide nanoparticles is primarily due to improved thermal conductivity, increased heat capacity, enhanced convective heat transfer, and beneficial particle interactions, all of which facilitate more efficient heat dissipation within the nanofluid.

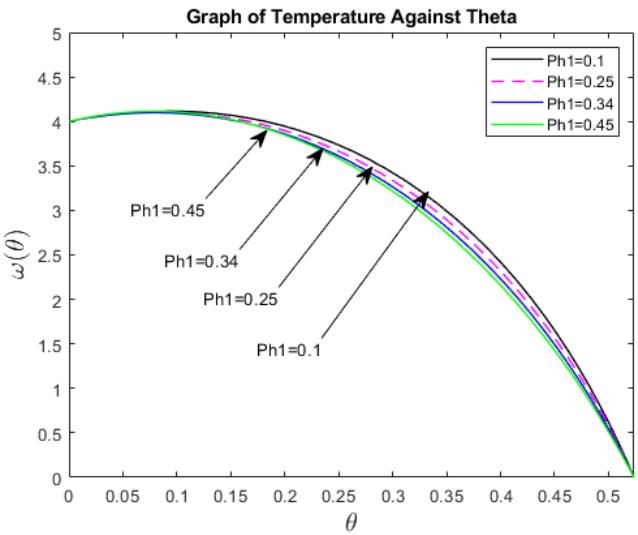

Fig. 15. Graph of temperature for varying Volume fraction of Aluminium Oxide.

As observed in figure (16), the increase in temperature profiles with a higher volume fraction of copper nanoparticles is mainly due to the combined effects of lower specific heat capacity, potential agglomeration leading to localized heating, and changes in heat dissipation dynamics, which create higher temperature regions within the nanofluid.

C. *Effects of Flow Parameters on Concentration*

From Figure 17, it is observed that an increase in Reynolds number leads to an increase in concentration profiles. This is because an increase in the Reynolds number corresponds to an increase in fluid velocity. The increase in velocity enhances the mixing within the fluid, which promotes the better dispersion of nanoparticles. As a result, the nanoparticles are more uniformly distributed throughout the flow, leading to higher concentration profiles.

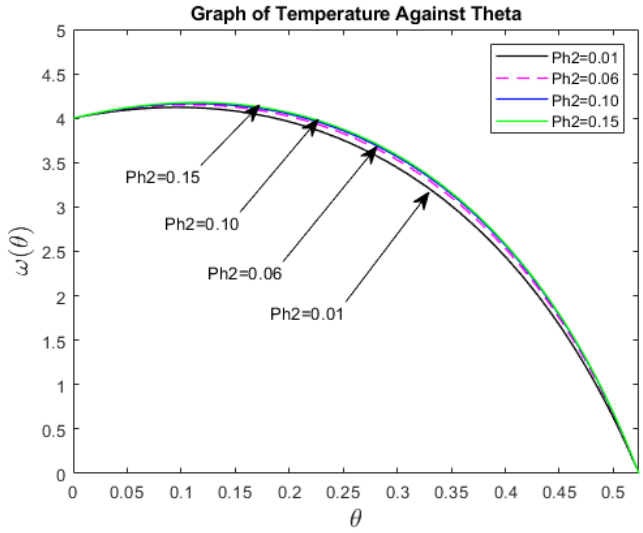

Fig. 16. Graph of temperature for varying Volume fraction of Copper.

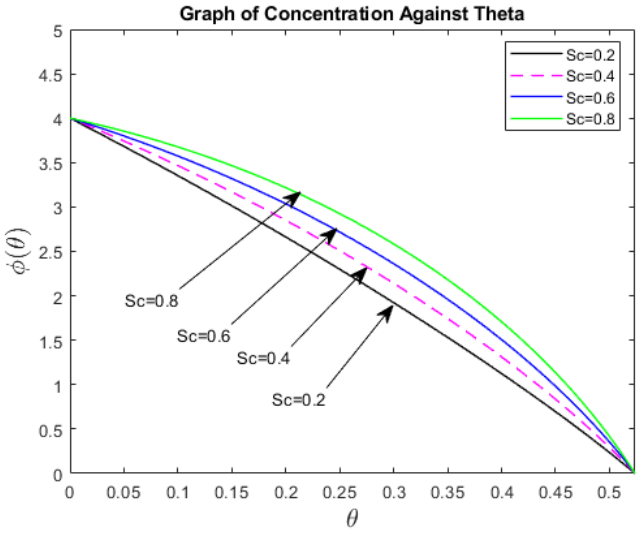

Fig. 18. Graph of concentration for varying Schmidt number.

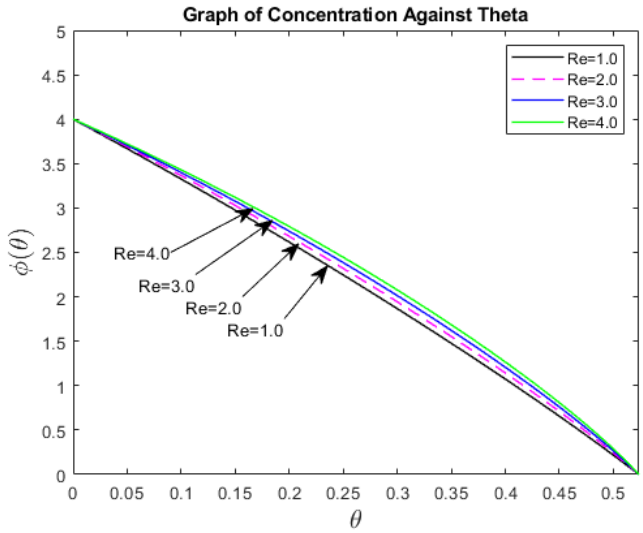

Fig. 17. Graph of concentration for varying Reynolds number.

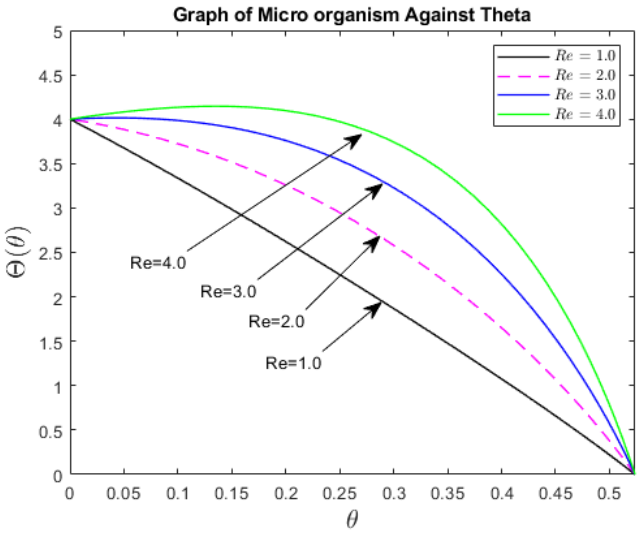

Fig. 19. Graph of microorganism density for varying Reynolds number.

In Figure 18, it is seen that an increase in the Schmidt number leads to an increase in the concentration profile. An increase in the Schmidt number corresponds to a decrease in the diffusivity of the DD mass due to their inverse relationship. A decrease in mass diffusivity implies reduced movement of nanoparticles, which decreases their dispersion within the fluid. As a result, the concentration of nanoparticles decreases locally, leading to an increase in the overall concentration of the fluid.

D. Effects of Flow Parameters on Microorganism Concentration

From Figure 19, it is observed that an increase in Reynolds number leads to an increase in microorganism concentration. As the Reynolds number increases, the fluid velocity also increases. This higher velocity enhances the mixing and dispersion of substances within the fluid. Consequently, the improved mixing results in a more uniform distribution of microorganisms throughout the fluid, leading to an increase in microorganism density.

From Figure 20, it is observed that an increase in the chemical reaction parameter leads to a decrease in the concentration of microorganisms. This is because certain chemical reactions produce by-products or reactants that are toxic to microorganisms. Gyrotactic microorganisms can respond by avoiding areas with high concentrations of toxins, using their directed movement capabilities to navigate away from harmful regions. This avoidance behavior can lead to a decrease in microorganism density in areas where chemical reactions result in elevated toxicity levels.

From Figure 21, it is observed that an increase in Schmidt number leads to an increase in microorganism density. The Schmidt number, Sc, is a dimensionless parameter that indicates the relative importance of momentum diffusion to mass diffusion. An increase in Sc implies that momentum diffusion dominates over mass diffusion.

As a result, microorganisms experience enhanced thermophoretic forces, which drive them toward regions of higher temperature. This movement increases the concentration of microorganisms in these hotter regions, leading to a higher overall microorganism density.

From Figure 22, it is observed that an increase in bioconvection Lewis number leads to a decrease in microorganisms density profile. The bioconvection Lewis number represents the ratio of diffusion to bioconvection effects. When the Lewis number increases, it implies that diffusion becomes relatively stronger compared to bioconvection. Therefore, as the bioconvection Lewis number increases, microorganisms are more likely to disperse due to diffusion.

From Figure 23, it is observed that microorganism density profile decreases with an increase in Peclet number. The Peclet number is defined as advective over a diffusive transport rate. The decrease in microorganism density with an increase in the Peclet number is because a rise in Peclet Number enhances the motion of the

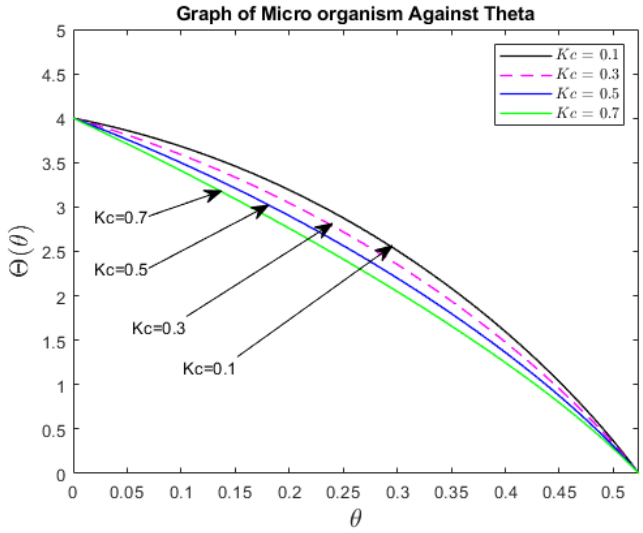

Fig. 20. Graph of microorganism density for varying chemical reaction parameter.

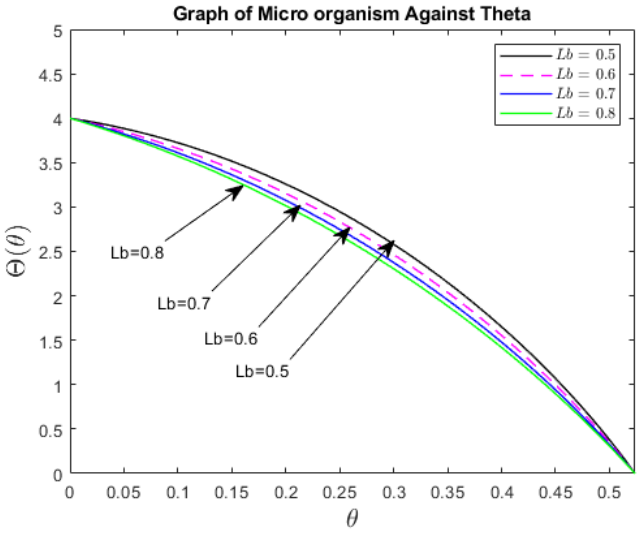

Fig. 22. Graph of microorganism density for varying microbial Lewis number.

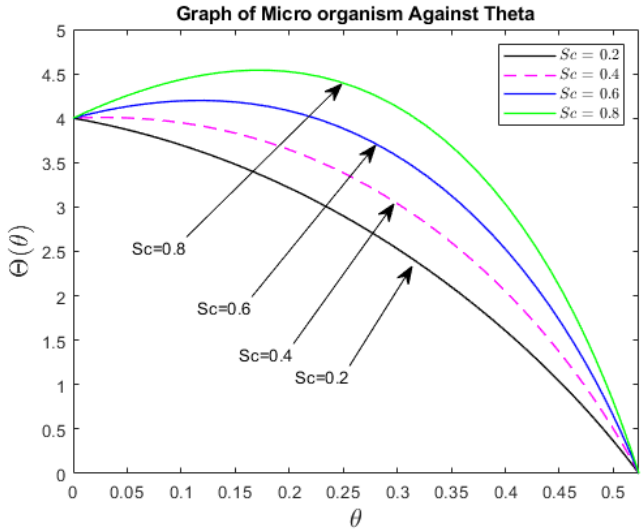

Fig. 21. Graph of microorganism density for varying Schmidt number.

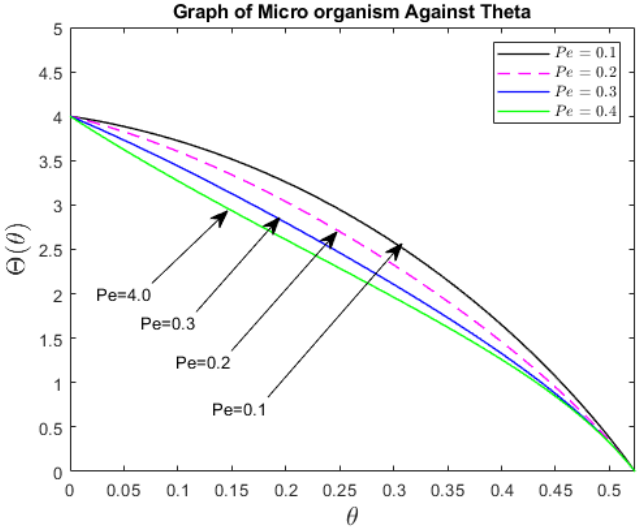

Fig. 23. Graph of microorganism density for varying Peclet number.

fluid particles, inducing a decline in the thickness of gyro-tactic microorganism.

From figure (24), the increase in aluminum oxide volume fraction leads to higher microorganism density through several mechanisms. First, aluminum oxide enhances the availability of nutrients in the surrounding environment, promoting the growth and proliferation of microorganisms. Its high surface area provides more sites for microbial attachment, resulting in a greater local density of microbes around the particles. Additionally, the presence of Aluminium oxide stabilizes microbial communities in fluid mediums, preventing washout and contributing to increased density. From figure (25), the increase in copper nanoparticle volume fraction leads to a higher microorganism density profile through several mechanisms. First, copper enhances nutrient availability in the surrounding environment, promoting microbial growth. Second, its antimicrobial properties create a selective environment that favors the growth of Gyro-tactic microorganisms that thrive in the presence of copper.

VIII. Summary and Conclusions

In this research, we have developed a thorough model for multi-phase hybrid gyro-tactic nanofluid flow through a porous convergent pipe with injection and suction. Our model accounts for various critical factors such as fluid incompressibility, non-Newtonian behavior, and the nonlinear relationship between viscosity and the tangential direction. The angle of inclination of the pipe is considered, and oil and water are treated as immiscible fluids separated by a smooth interphase. To ensure model accuracy, we meticulously adjust the volume fraction of each hybrid nanoparticle.

Our model comprises simultaneous governing equations for continuity, momentum conservation, energy, nanoparticle concentration, and microorganism density. Initially, nonlinear partial differential equations are transformed into nonlinear ordinary differential equations via similarity transformations. Subsequently, we linearize and discretize these ordinary differential equations using the spectral relaxation method, followed by simulation in MATLAB.

From our research, several key conclusions emerge:

(i) It is imperative to model oil recovery as two immiscible fluids, oil and water, due to their unique characteristics. We observe that the velocity of the fluid generally increases with certain flow parameters, such as Reynolds number, Thermal Grashof number, and Mass Grashof number.

(ii) The fluid temperature tends to rise with certain flow parameters, including Reynolds number, Eckert number, Unsteadiness parameter, thermal Grashof number, microbial Grashof number, and Joule heating parameter. Conversely, it decreases with increasing values of the chemical reaction parameter and Radiation parameter.

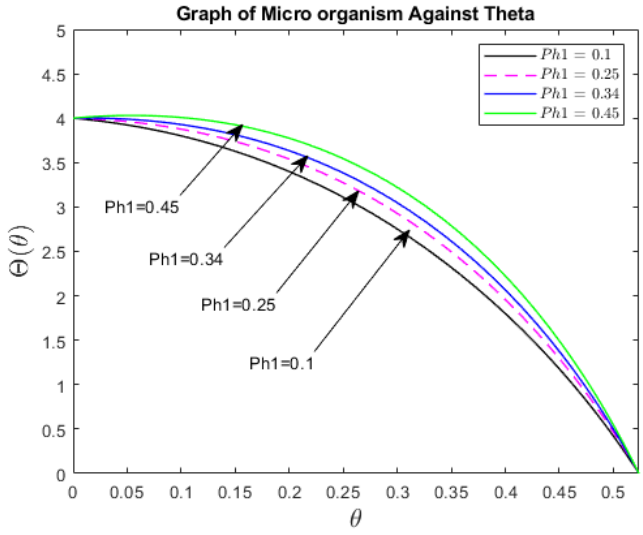

Fig. 24. Graph of microorganism density for varying Volume fraction of Aluminium Oxide.

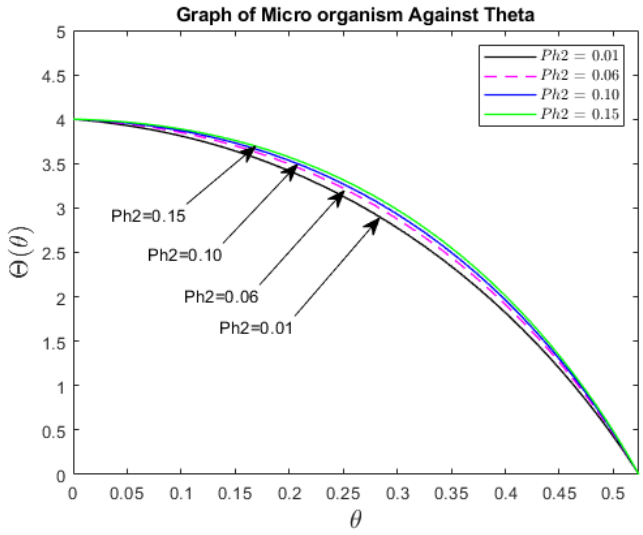

Fig. 25. Graph of microorganism density for varying Volume fraction of Copper.

(iii) The presence of gyro-tactic microorganisms plays a vital role in enhancing both the velocity and temperature of the fluid, essential elements for optimizing the oil recovery process. Increasing the density of these microorganisms emerges as a crucial strategy for engineers aiming to maximize oil yield. By doing so, engineers can effectively boost fluid velocity, promoting better fluid movement within the reservoir.

(iv) The heightened microbial density contributes to elevating the fluid temperature, which is instrumental in facilitating enhanced oil recovery. Thus, prioritizing the augmentation of microorganism density emerges as a paramount consideration for engineers seeking to optimize oil recovery operations and achieve higher yields.

(v) The concentration of the hybrid nanoparticles increases with an increase in Reynolds number and Schmidt number. However, it decreases with an increase in the chemical reaction parameter and the thermophoresis parameter.

(vi) The microorganism density increases with an increase in Reynolds number and Schmidt number. However, it decreases with an increase in chemical reaction parameter, thermophoresis parameter, microbial Lewis number and Peclet number.

IX. Recommendation to Engineers

1) Invest in technologies that allow the precise control and manipulation of flow parameters such as Reynolds number, Hartman number, and Grashof numbers to optimize fluid velocity and temperature for enhanced oil recovery.
2) Develop infrastructure to support the use of hybrid nanofluids in oil recovery operations, ensuring proper handling and application to maintain their stability and effectiveness.
3) Encourage regulatory frameworks that support the integration of advanced fluid models which consider non-Newtonian properties and variable viscosity into existing oil recovery processes.

References

[1] C. Nikolova and T. Gutierrez, "Use of microorganisms in the recovery of oil from recalcitrant oil reservoirs: Current state of knowledge, technological advances and future perspectives," *Frontiers in Microbiology*, vol. 10, pp. 29–96, 2020.

[2] S. Ahmad, M. Ashraf, and K. Ali, "Nanofluid flow comprising gyrotactic microorganisms through a porous medium," *Journal of Applied Fluid Mechanics*, vol. 13, no. 5, pp. 1539–1549, 2020.

[3] S. Alabdulhadi, I. Waini, S. E. Ahmed, and A. Ishak, "Hybrid nanofluid flow and heat transfer past an inclined surface," *Mathematics*, vol. 9, no. 24, pp. 31–76, 2021.

[4] R. T. Armstrong, D. Wildenschild, and B. K. Bay, "The effect of pore morphology on microbial enhanced oil recovery," *Journal of Petroleum Science and Engineering*, vol. 130, pp. 16–25, 2015.

[5] M. Azam, F. Mabood, and M. Khan, "Bioconvection and activation energy dynamisms on radiative sutterby melting nanomaterial with gyrotactic microorganism," *Case Studies in Thermal Engineering*, pp. 101–749, 2021.

[6] K. Behlülgil and I. Durgut, "Mathematical modeling of the soaking period in a microbial enhanced oil recovery application," *Energy sources*, vol. 25, no. 9, pp. 871–877, 2003.

[7] J. Chisholm, S. Kashikar, R. Knapp, M. Mclnerney, D. Menzies, and N. Silfanus, "Microbial enhanced oil recovery: Interfacial tension and gas-induced relative permeability effects," in *SPE Annual Technical Conference and Exhibition*. OnePetro, 1990.

[8] S. S. U. Devi and S. A. Devi, "Numerical investigation of three-dimensional hybrid cu–al2o3/water nanofluid flow over a stretching sheet with effecting lorentz force subject to newtonian heating," *Canadian Journal of Physics*, vol. 94, no. 5, pp. 490–496, 2016.

[9] D. Guzei, S. Ivanova, D. Platonov, and A. Pryazhnikov, "Computational study of enhanced oil recovery from a porous medium using nanosuspension," in *Journal of Physics: Conference Series*, vol. 1867, no. 1. IOP Publishing, 2022, pp. 012–025.

[10] M. F. Md Basir, M. Uddin, A. Md. Ismail, and O. A. Bég, "Nanofluid slip flow over a stretching cylinder with schmidt and péclet number effects," *AIP Advances*, vol. 6, no. 5, pp. 055–316, 2016.

[11] S. Mehryan, F. Moradi Kashkooli, M. Soltani, and K. Raahemifar, "Fluid flow and heat transfer analysis of a nanofluid containing motile gyrotactic micro-organisms passing a nonlinear stretching vertical sheet in the presence of a non-uniform magnetic field; numerical approach," *PloS one*, vol. 11, no. 6, pp. 157–598, 2016.

[12] C. Morel, "Mathematical modeling of disperse two-phase flows," 2015.

[13] K. Muhammad, T. Hayat, and A. Alsaedi, "Heat transfer analysis in slip flow of hybrid nanomaterial (ethylene glycol+ ag+ cuo) via thermal radiation and newtonian heating," *Waves in Random and Complex Media*, pp. 1–21, 2021.

[14] W. N. Mutuku and O. D. Makinde, "Hydromagnetic bioconvection of nanofluid over a permeable vertical plate due to gyrotactic microorganisms," *Computers & Fluids*, vol. 95, pp. 88–97, 2014.

[15] N. I. Nima, S. Salawu, M. Ferdows, M. Shamshuddin, A. Alsenafi, and A. Nakayama, "Melting effect on non-newtonian fluid flow in gyrotactic microorganism saturated non-darcy porous media with variable fluid properties," *Applied Nanoscience*, vol. 10, pp. 3911–3924, 2020.

[16] A. Raees, H. Xu, Q. Sun, and I. Pop, "Mixed convection in gravity-driven nano-liquid film containing both nanoparticles and gyrotactic microorganisms," *Applied Mathematics and Mechanics*, vol. 36, no. 2, pp. 163–178, 2015.

[17] S. Shaw, S. S. Motsa, and P. Sibanda, "Magnetic field and viscous dissipation effect on bioconvection in a permeable sphere embedded in a porous medium with a nanofluid containing gyrotactic microorganisms," *Heat Transfer—Asian Research*, vol. 47, no. 5, pp. 718–734, 2018.

[18] L. Zhang, M. Arain, M. Bhatti, A. Zeeshan, and H. Hal-Sulami, "Effects of magnetic reynolds number on swimming of gyrotactic microorganisms between rotating circular plates filled with nanofluids," *Applied Mathematics and Mechanics*, vol. 41, no. 4, pp. 637–654, 2020.

[19] S. A. Hussaini, R. Mohammad, G. M. Reddy, and S. Mustafa, "An inclined mhd and diffusive thermo effects on radiative viscoelastic periodic flow through porous medium channel." *IAENG International Journal of Applied Mathematics*, vol. 54, no. 8, pp. 1490–1498, 2024.

[20] S. Sharma and N. Prabhakar, "Numerical simulation of generalized fitzhugh-nagumo equation by shifted chebyshev spectral collocation method," *IAENG International Journal of Applied Mathematics*, vol. 54, no. 7, pp. 1371–1383, 2024.

[21] G. Buzuzi, M. Magodora, M. T. Kudinha, W. M. Manamela, and M. H. Mambo, "Steady mhd williamson nanofluid flow past an inclined stretching sheet in the presence of heat generation, chemical reaction and aligned magnetic field." *IAENG International Journal of Applied Mathematics*, vol. 54, no. 6, pp. 1125–1135, 2024.

[22] G. Buzuzi, M. T. Kudinha, and W. M. Manamela, "Effective prandtl number, hall currents, soret, and dufour effect on mhd flow past an inclined stretching sheet with aligned magnetic field and heat generation," *IAENG International Journal of Applied Mathematics*, vol. 53, no. 4, pp. 1201–1210, 2023.

[23] N. Nithya and B. Vennila, "The flow past a non-isothermal shrinking sheet with the effects of thermal radiation and heat source/sink," *IAENG International Journal of Applied Mathematics*, vol. 53, no. 4, pp. 1548–1559, 2023.

[24] G. Buzuzi, "Impact of channel slope, variable magnetic field and effective prandtl number on mhd maxwell fluid in the presence of heat generation and thermophoresis." *IAENG International Journal of Applied Mathematics*, vol. 53, no. 4, pp. 1637–1647, 2023.

[25] M. N. Othman, A. Jedi, and N. A. A. Bakar, "Mhd flow and heat transfer of hybrid nanofluid over an exponentially shrinking surface with heat source/sink," *Applied Sciences*, vol. 11, no. 17, pp. 81–99, 2021.

[26] M. Akhavan-Behabadi, F. Hekmatipour, S. Mirhabibi, and B. Sajadi, "Experimental investigation of thermal–rheological properties and heat transfer behavior of the heat transfer oil-copper oxide (hto-cuo) nanofluid in smooth tubes," *Experimental Thermal and Fluid Science*, vol. 68, pp. 681–688, 2015.

[27] S. Mukhopadhyay, "Slip effects on mhd boundary layer flow over an exponentially stretching sheet with suction/blowing and thermal radiation," *Ain Shams Engineering Journal*, vol. 4, no. 3, pp. 485–491, 2013.

[28] A. Mavi and T. Chinyoka, "Finite volume computational analysis of the heat transfer characteristic in a double-cylinder counter-flow heat exchanger with viscoelastic fluids," in *Defect and Diffusion Forum*, vol. 424. Trans Tech Publ, 2023, pp. 19–43.

[29] V. Ojiambo, M. Kinyanjui, and M. Kimathi, "A study of two-phase jeffery hamel flow in a geothermal pipe," 2018.

[30] J. Nagler, "Jeffery-hamel flow of non-newtonian fluid with nonlinear viscosity and wall friction," *Applied Mathematics and Mechanics*, vol. 38, pp. 815–830, 2017.

[31] L. N. Trefethen, *Spectral methods in MATLAB*. SIAM, 2000.

[32] N. S. Khan, T. Gul, M. A. Khan, E. Bonyah, and S. Islam, "Mixed convection in gravity-driven thin film non-newtonian nanofluids flow with gyrotactic microorganisms," *Results in physics*, vol. 7, pp. 4033–4049, 2017.